SPECTRUM SEPARATION FOR BRAIN TUMOR

MAGNETIC RESONANCE SPECTROSCOPY IMAGING

by

YUZHUO SU

A dissertation submitted to the Graduate Faculty in Biomedical Engineering in partial fulfillment of the requirements for the degree of Doctor of Philosophy, The City University of New York

2009

This manuscript has been read and accepted for the
Graduate Faculty in Biomedical Engineering in satisfaction of the
dissertation requirement for the degree of Doctor of Philosophy.

Lucas C. Parra

Date — Chair of Examining Committee

Mumtaz Kassir

Date — Executive Officer

Professor Marom Bikson

Professor Luis Cardoso

Professor Susannah Fritton

Dr. Sasan Karimi
Supervision Committee

THE CITY UNIVERSITY OF NEW YORK

ABSTRACT

SPECTRUM SEPARATION FOR BRAIN TUMOR

MAGNETIC RESONANCE SPECTROSCOPY IMAGING

by

Yuzhuo Su

Advisor: Lucas C. Parra

Altered metabolic activity in cancerous tissues leads to abnormal metabolite concentrations, which are reflected in abnormal spectral profiles in magnetic resonance spectroscopic imaging (MRSI). Currently, MRSI is utilized in conjunction with MRI to diagnose brain tumors. However, spectral profiles often show increased variability which limits the diagnostic potential of MRSI.

This thesis addresses this problem by quantifying the abundance (volume fraction) within a voxel for each tissue type instead of the conventional estimation of metabolite concentrations from spectral resonance peaks. This "spectrum separation" method simultaneously decomposes the observed spectra of multiple voxels into abundance distributions and constituent spectra.

Our results show that the proposed method can successfully extract spectral profiles consistent with different tissue types. We confirmed the physiological and clinical relevance

of the extracted spectra by correlating the analysis results with pathologically proven tumors. The results demonstrate reduced cross-subject variability, which leads to improved discrimination between high and low-grade gliomas.

The accuracy of the estimated abundances was validated on phantom data. The results indicate that the method correctly decomposes the observed data into constituent spectra corresponding to the different solutions with their specific metabolite concentrations. It validated the interpretation of abundance estimates as partial volume fraction and established bias and confidence intervals for its estimates.

Furthermore, we explored the potential of NMF in characterizing tissue heterogeneity. Our results showed that if sufficient diversity is apparent, our method can decompose MRSI data into multiple constituent spectra to capture tissue heterogeneity by modifying the number of the underlying sources.

We also tested semi-nonnegative matrix factorization (semi-NMF), a generalized factorization algorithm that allows mixed data matrix, for spectrum separation. Our results indicate that once the data has sufficient quality, semi-NMF is better suited for MRSI data.

Taken together, this thesis validated the physiological and clinical relevance of components extracted from brain tumor MRSI indicating that spectral separation of MRSI via NMF algorithm is not simply a mathematical decomposition but is clinically and physiologically meaningful. These additional physiologically relevant components obtained from the data can provide doctors with more clinical information and thus improve the diagnostic effectiveness of MRSI.

DEDICATION

I dedicate this thesis to the memory of my mother, Guifang Lei, who had always believed in me, supported me and loved me. She is my constant source of inspiration. I hope my achievement will complete the dream that she had for all those years.

ACKNOWLEDGEMENTS

I am indebted to my advisor and supervisor, Professor Lucas C. Parra, for his endless support, encouragement and advice, for providing me with a stimulating environment that allowed me to grow into an independent researcher, for leading me into medical imaging, an interdisciplinary and challenging field of research, and for always giving me confidence and guiding me with patience and building the foundation of my future career. His positive attitude with which he approaches any challenge has always been inspirational. It has not always been an easy road, but he has been an anchor of support throughout all these years.

I would like to give my special thanks to my rotation mentor and collaborator Professor Marom Bikson for his guidance and help, for introducing me into the field of neural engineering, and for his efforts to teach me laboratory technologies and train me to be an experimentalist.

I am grateful to our collaborators Dr. Wei Huang, Dr. Sasan Karimi and Dr. Sunitha B. Thakur from Memorial Sloan-Kettering Cancer Center (MSKCC) for providing data, clinical information and for their constructive suggestions; Dr. Paul Sajda, Dr. Truman Brown, and Dr. Shuyan Du from Columbia University for their help with the algorithm and data analysis. And thanks also to Dr. Wei Yuan from The City College of New York (CCNY) for his help in phantom study. This project could not exist without any of them.

My gratitude to the members of my thesis committee: Professor Marom Bikson (CCNY), Professor Luis Cardoso (CCNY), Professor Susannah Fritton (CCNY) and Dr. Sasan Karimi (MSKCC). They have been a source of encouragement and advice that have contributed a great deal in the course of my Ph.D. work.

My fellow lab members of Neural Engineering Lab have been invaluable to me not only in helping me with the research work, but also in making the lab a fun and exciting place to work at. My thanks to Xiang Zhou, Joao Da Custodia Dias, Christoforos Christoforou, Thomas Radman, Jake Vaynshteyn, Je Hi An, Abhishek Datta, Davide Reato, and Jacek Dmochowski. Thanks to them for being a great source of support and friendship.

Heartfelt thanks to my family. I thank my husband Jianjun Zhang, who has been always standing by me with his patience, understanding, support, and most of all love. Without him the completion of this work would not have been possible. I thank my parents for their unfaltering understanding, endless support and unconditional love. They have never stopped believing in me while never gave me any undue pressure. They have always provided me with every opportunity to succeed at their best. I am indebted to their sacrifice for a lifetime.

CONTENTS

List of Figures

List of Tables

Chapter 1 Research Motivation and Thesis Overview

Although MRSI has become an important imaging modality in brain tumor diagnosis, the clinical utility of MRSI has been limited by the significant variability of the *in vivo* spectra which can be introduced by many factors such as tumor heterogeneity, partial volume coverage, measurement noise, etc. A spectrum separation approach which represents each spectrum as a linear combination of constituent spectra has the potential to reduce the spectral variability in two ways: first, assigning abundance values to each voxel captures and compensates for the variability due to partial volume; second, computing a single spectrum that is applicable across many voxels reduces estimation variance due to measurement noise.

The NMF algorithm discussed in this thesis is a blind source separation algorithm. The approach is unsupervised, which makes it a sound approach in the study of MRSI data, given the source signals (tissue specific spectra) are usually not observed and it is difficult to model the mixture of underling source signals within sample voxels. By adding a positivity constraint in the updating rules of the NMF approach for source separation, the lack of prior knowledge about mixing is compensated by a statistically strong but physically plausible assumption of the underlying sources, which makes the algorithm a versatile tool for statistical spectral analysis.

Previously, Sajda et al. successfully applied a variant of the NMF algorithm to brain MRSI data (1). The algorithm automatically decomposes the recorded MRSI data into two non-negative matrices representing (a) the underlying tissue-specific spectral patterns and (b) the spatial distribution of the corresponding metabolite concentrations. Their results showed that the spectral profiles and their spatial distributions are consistent with different tissue types such as necrotic and proliferative regions, normal brain, and skull (1). However, the physical reality of this mathematical decomposition and its physiological and clinical relevance are not well established. The questions that need to be answered are firstly if the proposed spectrum separation method extracts physiologically meaningful constituent spectra (***S***). And secondly if it is reasonable to interpret the abundance estimates (***A***) as volume fraction and how accurate their estimation is.

This thesis addresses these questions by performing the following analysis:

1. The physiological and clinical relevance of the extracted spectra ***S*** is confirmed in Chapter 7 and 8 by correlating the analysis results with pathologically proven tumor grades from 20 patients using the model with two basic sources, i.e. normal and tumor tissue. The results demonstrate reduced cross-subject variability, which is reflected in improved discrimination between high and low-grade gliomas.

2. To validate the interpretation of abundance estimates, ***A***, as partial volume fraction, we performed a phantom study. Accuracy of the abundance estimates is quantified in Chapter 8 by establishing bias and confidence intervals for its estimates for

the phantom data. Also, the thesis discusses in detail the possible reasons for the systematic bias and proposed a way for further evaluation.

Validation of the physiological and clinical relevance of the extracted spectra $\boldsymbol{A}$ and $\boldsymbol{S}$ (Chapter 8) is the major contribution of this thesis.

In addition to the main goal of validating the physiological and clinical relevance of the decomposition, this thesis will also discuss several topics related to MRSI spectrum separation as follows.

A problem of multi-voxel methods is that they assume constituent spectra to be the same across voxels, thus require careful correction of deviations such as phase errors and frequency shifts. Therefore for our analysis it was necessary to redevelop the corresponding data conditioning routines. Chapter 4 discusses in details each step of the preprocessing procedures. Especially in the frequency domain, a theoretical derivation is performed in Chapter 5 to validate the logic behind each procedure of the frequency domain corrections.

Voxel selection is a critical step for spectral analysis. Inclusion of noisy or distorted spectra has a detrimental effect for all the statistics-based factorization algorithms. In this thesis the limitations of the method in terms of signal-to-noise ratio (SNR) were evaluated in Chapter 6. The minimum required SNR for the proposed spectrum separation approach was quantified on simulated data.

Spectral separation with NMF extracts homogeneous spectra from normal and tumor tissues. But this assumption might not be true, especially for tumor spectra which usually do not always show a unique and stable spectral pattern. The pattern of tumor spectra may differ for tumors of different grades and types, even within the same tumor due to the heterogeneity of tumor tissue itself. Chapter 9 shows that the data can be decomposed into multiple constituent spectra in case of inhomogeneous spectra within the abnormal tissues, which demonstrates the potential of the proposed approach in characterizing tissue heterogeneity.

As discussed earlier, with specific application of the NMF approach to the MRSI data, one problem is that, due to random noise in MRSI data, the observations $\boldsymbol{X}$ can have negative values. The current solution is to apply a threshold (force all negative values to be zero) or to use absolute spectra, which will introduce certain degree of non-linearity to the system. Thus improvement of the NMF algorithm is necessary for MRSI data analysis to provide biochemically meaningful and physically interpretable solutions. This thesis explored a generalized factorization algorithm, semi-NMF to perform the spectrum separation. It allows the data matrix to have mixed signs, which makes the algorithms better suited for MRSI data as compared to the current NMF algorithm. This thesis developed the processing routine by using the semi-NMF and confirmed the applicability of the semi-NMF algorithm for MRSI data. The accuracy of the decomposition is quantified in the Chapter 10.

Note that other pressing problems of MRSI related to data acquisition are not explicit focus of this work. For instance, an inhomogeneous magnetic field can lead to

significant distortions of the spectral data. In particular water and lipid suppression are complicated by this inhomogeneity. The effects on the acquired data can be partially compensated by appropriate data processing as will be explained in Chapter 4. Other issues related to pulse sequence design such as the rigidity of the acquisition volume, or the partial coverage of a region of interest are beyond the scope of this work.

Part of the research work presented in this thesis was published in (2-7).

Chapter 2 Introduction

2.1 Magnetic Resonance Imaging and Magnetic Resonance Spectroscopy Imaging

2.1.1 Magnetic Resonance Imaging

Structural magnetic resonance imaging (MRI) is a important imaging modality used in medical settings to produce high quality images of the inside of the human body. MRI provides superior soft-tissue contrast with flexible data acquisition protocols that highlight several different properties of the tissue. It has become the imaging of choice for evaluating brain morphology and plays a critical role in brain tumor diagnosis, guiding biopsies and surgical resection, as well as planning radiotherapy, evaluating response to therapy and monitoring recurrence (8,9).

MRI is based on a physics phenomenon discovered in the 1930s, called nuclear magnetic resonance (NMR). Felix Bloch working at Stanford University and Edward Purcell from Harvard University, both of whom were awarded the Nobel Prize in 1952, discovered the magnetic resonance phenomenon independently in 1946. In the period between 1950 and 1970, NMR was developed and used to obtain microscopic chemical and physical information about molecules. In 1970, Raymond Damadian, a medical

doctor and research scientist, discovered the basis for using magnetic resonance imaging as a tool for medical diagnosis. He found that the relaxation times of different tissues vary, and that cancerous tissue emits response signals that last much longer than non cancerous tissue. In 1974, the world's first patent issued in the field of NMR was granted to him for his idea of using magnetic resonance imaging as a tool for medical diagnosis, entitled "Apparatus and Method for Detecting Cancer in Tissue". By 1977, he completed construction of the first whole-body MRI scanner.

The basis of current MRI techniques using phase and frequency encoding, and the Fourier Transform were proposed by Richard Ernst in 1975. His achievement in pulsed Fourier Transform NMR and MRI was rewarded him with the Nobel Prize in Chemistry in 1991. In 1993 functional MRI (fMRI) was developed. This technique allows the mapping of the various regions of the human brain responsible for thought and motor control.

In 2003, Paul C. Lauterbur from the University of Illinois at Urbana-Champaign and Peter Mansfield from the University of Notingham were awarded jointly the Nobel Prize in Physiology or Medicine for their discoveries concerning “magnetic resonance imaging”. The main contribution of Paul Lauterbur in developing modern MRI is his discovery of the possibility to create a two-dimensional picture by introducing gradients in the magnetic field. By analysis of the characteristics of the emitted radio waves, he could determine their origin. This made it possible to build up two-dimensional pictures of structures that could not be visualized with other methods. Peter Mansfield further developed the utilization of gradients in the magnetic field. He showed how the signals

could be mathematically analyzed, which made it possible to develop a useful imaging technique. Peter Mansfield also showed how extremely fast imaging could be achievable. This became technically possible within medicine a decade later.

MRI is now a routine method within medical diagnostics. Worldwide, more than 60 million investigations with MRI are performed each year (10), and the method is still in rapid development. MRI is often superior to other imaging techniques and has significantly improved diagnostics in many diseases. MRI has replaced several invasive modes of examination and thereby reduced the risk and discomfort for many patients. In dealing with brain tumors, the ability of MRI to provide pictures from various planes permits doctors to create a three-dimensional image of a tumor. The MRI detects varying signals emitted from normal and abnormal tissues, providing clear images of most tumors. Therefore, it has played an important role as a non-invasive modality for determining tumor extent, grading, and monitoring treatment and tumor re-occurrence. The specificity of MRI for initial diagnosis, however, is highly variable, between 30-90% depending on tumor type (11-14).

2.1.2 Magnetic Resonance Spectroscopy Imaging

Chemical Shift Imaging (CSI) is an image modality which was invented by Truman Brown in 1982 (15) using the same basic principles as in MRI. It measures high resolution nuclear magnetic resonance (NMR) spectra across a volume of tissue. CSI

assesses tissue function by obtaining information about the composition and spatial distribution of cellular metabolites.

In the context of human CSI, proton (^{1}H) magnetic resonance spectroscopy imaging (MRSI) is of particular interest. In the clinical setting, MRSI can be obtained during the same session as the MRI examination, therefore providing both morphological and metabolic imaging with minimal additional time. Proton MRSI is mainly employed in the studies of the brain, and the major brain metabolites which can be detected include choline (Cho, 3.2 ppm), creatine (Cr, 3.0 ppm), N-acetyl aspartate (NAA, 2.0 ppm), and lactate and/or lipids (Lac, 1.3 ppm). *In vivo* MRSI allows non-invasive characterization and quantification of molecular markers with clinical utility for improving detection, identification, and treatment for a variety of diseases, most notably brain tumors.

2.2 Brain Tumors

2.2.1 Epidemiology

Brain tumors are a diverse group of diseases characterized by the abnormal growth of tissue contained within the skull. There are more than 200,000 new brain tumor cases in the United States each year (16). Brain tumors have surpassed acute lymphoblastic leukemia (ALL) and become the leading cause of cancer death in children under the age of 20 (17). They are the third leading cause of cancer death in young adults ages 20-39. Although as many as 70% of children diagnosed with primary brain tumors will survive, they are often left with long-term side effects (18).

2.2.2 Classification

There are two types of brain tumors: primary brain tumors and metastatic brain tumors. Primary tumors are tumors that originate in the brain. Among more than 200,000 new cases of brain tumors diagnosed in the United States each year, 40,000 cases are primary brain tumors (17). Primary brain tumor rarely spreads beyond the central nervous system, and death usually results from uncontrolled tumor growth within the limited space of the skull. Primary brain tumors can be grouped into benign tumors and malignant tumors. Both types take up space in the brain and may cause serious symptoms (e.g., vision loss, hearing loss, paralysis) and complications (e.g., stroke). In contrast to primary brain tumors, metastatic (secondary) brain tumors are tumors that have migrated from other parts of the body. Metastatic brain tumors are more prevalent than primary tumors and they indicate advanced disease and poor prognosis. All metastatic brain tumors are, by definition, malignant.

2.2.3 Grading

Based on the malignancy of the tumor, brain tumors are graded to facilitate communication, to plan treatment, and to predict outcome. Nowadays, most medical centers use the World Health Organization (WHO) classification system for this purpose (19).

Grade I tumors are the least malignant tumors, which grow slowly and appear almost normal microscopically. These tumors are often associated with long-term

survival because they could be potentially cured by surgery alone. However, they can be life-threatening if they are inaccessible by surgery. Grade II tumors grow slightly faster than grade I tumors and have a slightly abnormal microscopic appearance. These tumors may invade surrounding normal tissues, and may recur as higher-grade tumors. Grade III tumors are all malignant. Tumor cells are apparently abnormal microscopically. They grow fast and often invade surrounding normal tissues. Recurrence rate is high for grade III tumors after resection and they often recur as grade IV tumors, which are the most malignant. Grade IV tumors proliferate rapidly and are often necrotic in the center. These tumors almost always invade wide area of surrounding normal tissues.

Malignant tumors may contain tumor cells of different grades. The overall grading is determined by the most malignant cells in the tumors, even if most of the tumor is lower grade. Some tumors undergo change. A benign growth might become malignant. In some tumors, a lower-grade tumor might recur as a higher-grade tumor.

2.2.4 Diagnosis of Brain Tumors

Early and accurate diagnosis is critical for minimizing the morbidity and mortality for brain tumors. Diagnosis of brain tumor usually involves several steps and may include a neurological examination, brain imaging scan(s), a biopsy and a resection.

1) Neurological Examination

When brain tumors are suspected, a series of neurological examination is usually performed to measure the basic status of the patient's nervous system and mental alertness. A basic neurological examination may include vision tests, hearing tests, smelling tests, sensation tests, balance and coordination tests, movement tests, mental status tests, memory tests, *et al*. Abnormal exams are suggestive of diseases and location. Imaging scans usually follows to confirm diagnosis.

2) Brain Scan(s)

The rapid development of brain imaging has had a dramatic impact on the diagnosis of brain tumors. Advances in imaging techniques are enabling doctors to produce remarkably detailed computer-screen images to evaluate structural abnormality and identify tumor-related complications.

Early imaging methods such as pneumoencephalography and cerebralangiography have been abandoned since those methods are invasive and sometimes dangerous. The most common scans for diagnosis and follow-up are computed tomography (CT) and magnetic resonance imaging (MRI).

● CT

CT imaging combines special x-ray equipment with sophisticated computers to produce a series of 2-D and 3-D cross-section pictures of the inside of the body. Characteristics of the internal structure of an object such as dimensions, shape, internal defects, and density are readily available from CT images. A CT scanner uses X-rays, a type of ionizing radiation, to acquire its images, making it a good tool for examining tissue composed of elements of a relatively higher atomic number than the tissue surrounding them, such as bone and calcifications (calcium based) within the body (carbon based flesh), or of structures (vessels, bowel). Compared with the regular x-ray exams, CT scans of internal organs, bone, soft tissue and blood vessels provide greater clarity and reveal more details. It can therefore provide more detailed information on head injuries, stroke, brain tumors and other brain diseases. Brain tumors often show up as hypodense (darker than brain tissue) mass lesions on cranial CT-scans. It often is used as a first imaging study in brain tumor investigations, although it is much less sensitive and specific than MRI (20).

● MRI

MR imaging uses a powerful magnetic field, radio frequency pulses and a computer to produce detailed pictures of organs, soft tissues, bone and virtually all other internal body structures. The images can then be examined on a computer monitor, printed or copied to CD. MRI does not use ionizing radiation (x-rays), on the other hand,

uses non-ionizing radio frequency (RF) signals to acquire its images and is best suited for non-calcified tissue. Brain tumors often appear either hypo- (darker than brain tissue) or isointense (same intensity as brain tissue) on T1-weighted scans, or hyperintense (brighter than brain tissue) on T2-weighted MRI. Perifocal edema also appears hyperintense on T2-weighted MRI. Detailed MR images allow physicians to better evaluate parts of the body and certain diseases that may not be assessed adequately with other imaging methods such as x-ray, ultrasound or CT. It is the most effective and common way for brain tumor diagnosis.

- Magnetic Resonance Spectroscopic Imaging (MRSI)

In vivo Magnetic Resonance Spectroscopy (MRS) is a specialized technique associated with MRI. It is a molecular imaging technique used to measure the levels of different metabolites in body tissue as biomarkers. It combines both spectroscopic and imaging methods to produce spatially localized spectra from within the sample or patient. In another word, MRS produces images depicting function rather than shape. This signature is used to diagnose certain metabolic disorders, especially those affecting the brain(21), as well as to provide information on tumor metabolism(22).

● Positron Emission Tomography (PET)

PET is a nuclear medicine imaging technique which produces a three-dimensional image or picture of functional processes in the body. In a PET scan, a low-dose of deoxyglucose that has been labeled with radioactive markers is injected into the patient. The PET scanner rotates around the patient's head, detecting the amount of radioactive sugar taken up by various parts of the brain. It provides a picture of the brain's activity, rather than its structure, by measuring the rate at which a tumor absorbs glucose (a sugar). The PET scan then sends this information to a computer, which creates a live image. PET is not routinely used for diagnosis of brain tumor but it can complement scanning information by suggesting tumor grade. It can also be used to gain more information about a tumor while a patient is undergoing treatment or if there is a recurrence (the cancer comes back after treatment).

These advanced imaging modalities are noninvasive procedures that can measure biological activity through the skull and reveal the living human brain at work. Each technique has its own advantages and each provides different information about brain structure and function. For this reason, doctors are increasingly conducting studies that integrate two or more techniques. For example, merging a PET scan image that shows activity at brain molecular sites, or receptors, with a highly detailed MRI image of brain structure can produce a composite image that makes it possible to identify more precisely where in the brain the activity is occurring. Due to the non-invasive and high-resolution manner of the brain imaging modalities, together with the rapid development of the

imaging technologies, medical imaging plays a more and more important role and has a more and more dramatic impact in the diagnosis of brain tumors.

3) Pathology

In current clinical practice, the pathologic diagnosis is still the gold-standard for brain tumor diagnosis and grading. A biopsy is a surgical procedure in which a sample of tissue is taken from the tumor site and examined under a microscope. The biopsy will provide information on types of abnormal cells present in the tumor. Biopsy is generally considered by many practitioners to be safe. But there has always been controversy over whether the act of obtaining a biopsy may allow the spread of cancerous cells to other areas of the brain. In contrast to a biopsy that merely samples a lesion, resection that samples a larger specimen may be performed if the tumor is accessible and the patient's general health is good. Examination of the full specimen would confirm the exact nature of the cancer (subclassification of tumor and histologic "grading") and reveal the extent of its spread. But studies have shown that it comes with significant risks including a 1.7% mortality rate (23) and 8% chance of other serious complications (14).

2.2.5 Treatment

The treatment of a brain tumor depends on a number of factors including the size, type, location, and grade of the tumor, whether it is cancerous, whether it has spread to

other parts of the central nervous system (CNS) or body, as well as the person's age and general health. Patients diagnosed with a CNS tumor generally need to seek treatment as soon as possible, because some tumors can grow quickly and cause severe symptoms. Surgery, radiotherapy and chemotherapy are commonly used therapies. In many circumstances, combination of two or three of above treatments are used to achieve the best response. Three types of standard treatment are used:

1) Surgery

Surgery is the treatment of choice for resectable brain tumors and is often the only treatment needed for a benign brain tumor. Surgery to the brain requires the removal of part of the skull. This operation is called a craniotomy. Whenever possible, the surgeon attempts to remove the entire tumor. If the tumor cannot be completely removed without damaging vital brain tissue, the surgeon may remove as much of the tumor as possible. Partial removal helps to relieve symptoms by reducing pressure on the brain and reduces the amount of tumor to be treated by radiation therapy or chemotherapy. There have been rapid advances in surgery for brain tumors including the use of cortical mapping and enhanced imaging systems to give surgeons more tools to plan and perform the surgery.

2) Radiation Therapy

Radiation therapy is the use of high-powered x-rays or other particles to damage cancer cells and stop/slow them from growing. It is often used to destroy tumor tissue that cannot be removed with surgery or to kill cancer cells that may remain after surgery. Radiation therapy is also used when surgery is not possible.

3) Chemotherapy

Chemotherapy is the use of drugs to kill cancer cells. Chemotherapy can be performed by using one drug or multiple drugs and can be given orally (by mouth), intravenously (IV, by vein), or directly into the tumor cavity. Systemic chemotherapy is delivered through the bloodstream, targeting cancer cells throughout the body. The goal of chemotherapy can be to slow the tumor's growth, or reduce symptoms, and destroy cancer cells remaining after surgery.

2.2.6 The Role of Imaging in the Treatment of Brain Tumors

Advanced imaging technologies are now being used not only for evaluating the morphologic and biologic alterations, but also for planning and conducting treatment strategies, a concept referred to as image-guided interventions. Image-guided interventions have involved in many fields such as surgery, lesion ablations, embolization of vascular defects, radiation treatment, or other therapies.

The contribution of advanced imaging for brain tumor treatment includes two primary areas: imaging for better understanding of biology of tumor and normal tissues; imaging for verification of treatment delivery.

Modern brain imaging methods, such as PET, CT, MRI/MRSI, have allowed development of many noninvasive or minimally invasive strategies in imaging of physiological, metabolic, and functional processes of tumors or normal tissues. Important biological aspects of tumors to be imaged include metabolite contents, the presence of hypoxia, and cell proliferation.

Imaging for validation and verification of treatment delivery is developing as imaging-based treatment where the imaging is performed in real-time or near real-time relative to the treatment process. The ability of modern imaging technologies in delivery detailed 3D images makes it possible to get distinct information on tumor localization. Such information is valuable for precise surgery and radiation therapy. Before surgery, it is important to know whether the tumor has infiltrated the surrounding tissues. MRI in particular can more exactly than other methods differentiate normal tissues from cancerous tissues and thereby contribute to improving surgery.

As discussed above, brain tumor treatment is becoming more and more image based. In addition to enhancing substantially the effectiveness of traditional approaches for establishing diagnosis and treatment, modern imaging methods have evolved into a comprehensive tool for evaluating and treating brain tumors. Among these imaging modalities, MRI/MRSI plays indispensable roles in diagnosis, treatment planning and treatment responses monitoring.

2.3 Magnetic Resonance Spectroscopy Imaging in Brain Tumor Diagnosis

Together with structural magnetic resonance imaging (MRI), MRSI can provide an integrated biochemical and morphological view of biological tissue and disease processes. The major brain metabolite peaks detectable in proton MRSI are choline (Cho, 3.2 ppm), creatine (Cr, 3.0 ppm), N-acetyl aspartate (NAA, 2.0 ppm), and lactate and/or lipids (Lac, 1.3 ppm). Peak area is used as a relative measure of the metabolite concentration. The relative signal intensity ratios of various metabolites (and their concentrations) show significant changes in various pathological conditions affecting the brain. In general, there are relatively high choline and lactate−lipid levels and relatively low NAA and creatine levels in the tumor (24-27).

NAA is the most prominent resonance in a proton spectrum resonating at 2 ppm. It is accepted as a neuronal marker (28). NAA is one important metabolite for the regulation of neuronal protein and neurotransmitter synthesis, and myelin production (29,30). The concentration of NAA will decrease with many insults to the brain, such as neoplasms, infarcts, epilepsy, and dementia (31).

Creatine resonates at 3.03 ppm representing the energy source (32). It often reduces in tumors (33,34), but the significance of decreased Cr in terms of tumor metabolism is not clear.

The peak for choline occurs at 3.2 ppm. Choline is a precursor of acetylcholine and a component of certain phospholipids and is involved in the synthesis and

degradation of cell membranes, and their concentration may be affected in disorders that influence membrane turnover. Therefore, increased choline probably reflects increased membrane synthesis and/or an increased number of cells, as seen in tumors (35,36) (Figure 1 and Figure2).

The lactate peak is at 1.32 ppm. The presence of lactate generally indicates that the normal cellular oxidative respiration mechanism is no longer in effect, and that carbohydrate catabolism is taking place (37). It is very low in normal tissue. Although nonspecific, increased Lac is often observed in tumor (38-40).

Normally brain tumor ^{1}H MR spectra are characterized by the signal intensity change of several important brain tissue types and metabolites. Figure 1 (41) shows an example of ^{1}H MRSI data from a patient of a glioblastoma overlaid on a T_2-weighted image spin−echo MRI. Figure 1a shows the voxels of the proton MRSI superimposed on the MRI image. The tumor tissue shows as hyperintensity. An example of ^{1}H MRS spectrum from solid tumor and healthy tissue is shown in Figure 1b. Compared with the spectrum from normal brain tissue, signal intensity of NAA is reduced while Cho is elevated in the tumor spectrum. Peak area is affected by the metabolite's relaxation time and varies proportionately with concentration. It is therefore used as a relative measure of metabolite concentration. The most consistent pattern observed in all types of brain tumors is an increased Cho and decreased NAA – a pattern which is now widely accepted as an indicator for neoplasia (42).

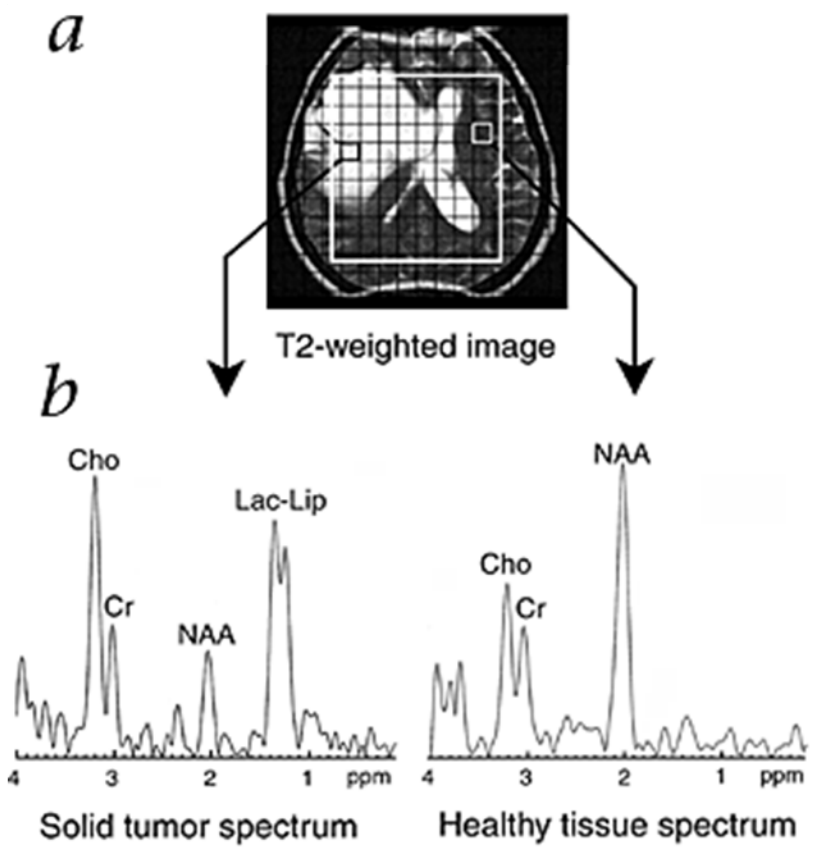

Figure 1: Example *in vivo* Proton MRSI data from De Edelenyi et al. (41)

1a, T_2-weighted image spin−echo MRI of a glioblastoma. The grid superimposed on the MRI image shows the voxels of the proton MRSI. The tumor tissue shows as hyperintensity. **1b**, ^1H spectra from two voxels located within the solid tumor and within the healthy tissue. The horizontal axes is in chemical shift units parts per million (ppm) and the vertical axes is scaled in the same arbitrary unit (A.U.).

2.3.1 Conventional Criteria of MRSI for Brain Tumors Diagnosis

Metabolite peak areas in conjunction with conventional MRI findings are used to determine the presence of tumor. A conventional quantitative criterion is the Cho-to-NAA index (CNI), which measures the ratio of the Cho peak area (or height) to the area (or height) of the Cr or NAA peak (42). Disregarding other variables such as patients' age

and locations of the voxels, a CNI mildly higher than 1 is generally considered abnormal but non-specific, and a CNI above 3 is likely to be a high-grade tumor.

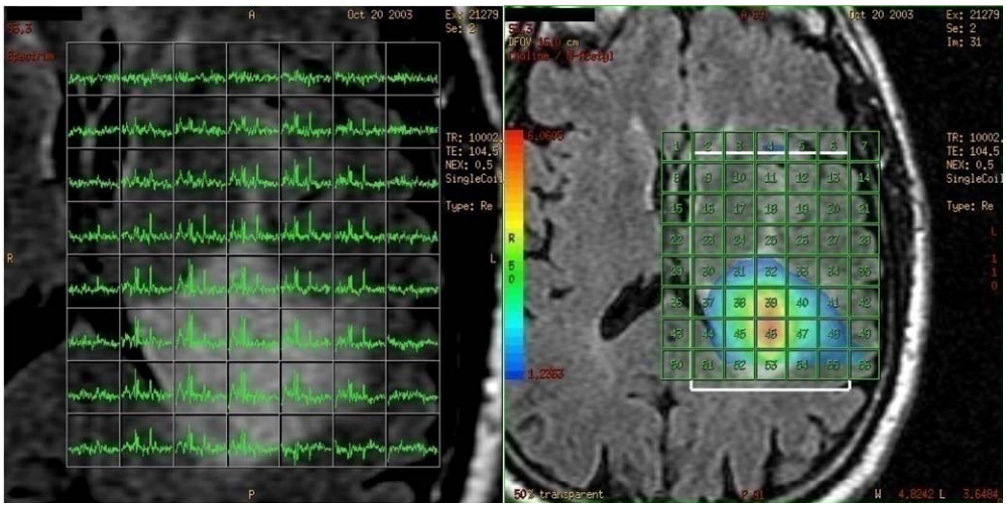

a b

Figure 2: Current display of MRSI data overlaid on a FLAIR image for a subject with an oligodendroglioma

2a: MR multi-voxel spectra overlaid on a FLAIR image showing the tumor as hyperintensity. Spectra in green show peaks of varying height embedded in background noise. Two of these peaks indicate the presence of Cho and NAA metabolite. **2b**: The color map shows the Cho/NAA concentration ratio. The zoomed region on the left corresponds to the green grid on the right.

Figure 2a shows ^{1}H MRSI data for a patient with an oligodendroglioma overlaid on a MRI Pre-contrast Fluid-Attenuated Inversion Recovery (FLAIR) image. The spectra from the tumor tissue (shown as hyperintensity in the FLAIR image) are characterized by increased resonance peaks of Cho, and decreased peaks of NAA. Figure 2b shows the corresponding CNI map in the tumor region. In the image, red is CNI6; yellow is CNI4; blue is CNI1.

In current clinical practice, CNI is usually used as a quantitative measure of the probability of spectroscopic abnormality. However, tumor heterogeneity, partial volume coverage, and measurement noise add significant variability to the spectra making this quantitative criterion difficult to use (43,44).

2.3.2 Spectral Mixtures and Its Implications in Clinical Practice

In current clinical setting, because of limitation in scanning time for data averaging, the common voxel size is about 1cc in order to achieve reasonable SNR. This relative large voxel often contains a combination of different tissue types, such as normal white or gray matter, necrotic or cystic tissue, tumor tissue of different grades, etc. Each tissue type can be viewed as having a characteristic spectral profile corresponding to the chemical composition of the tissue. In tumors, ^{1}H MRSI has shown that metabolites are heterogeneously distributed and in a given voxel multiple metabolites and tissue types may be present (45-47). The observed spectra are therefore a combination of different constituent spectra and are quite variable within and across subjects (43,44).

This heterogeneity creates two immediate practical problems:

A) Which spectrum should be selected for diagnosis given within-subject variability?

Often the spectra of voxels within a MRI contrast-enhancing region are considered. However, this may not always be appropriate as some tumors are non-

enhancing. In addition, the center of the enhancing region in large tumors may be necrotic, while the proliferative boundary may be distributed across multiple mixed voxels (44). It would be beneficial to have a separate spectrum for each constituent tissue type rather than for each voxel.

B) What is a consistent marker of a particular pathology given cross-subject variability?

Conventional spectral analysis estimates the relative concentrations of different metabolites by measuring the area of the resonance lines associated with each metabolite (48). Relative metabolite concentrations are then used as diagnostic index for decease. For example, CNI, as discussed above, measures how far the concentration ratio of Cho to NAA differs from the values of a normal brain (42). Many such relations can be defined including concentrations of other metabolites such as Lactate, Lipids, Glycine, Glutamate and Glutamine, myo-Inositol, assuming that the corresponding spectral lines are detectable above the background noise. However, given heterogeneity of tumor spectra it is difficult to define a strict relation between metabolite concentrations and pathology (43,44) even when using pattern analysis methods such as linear discriminant analysis (49).

2.4 Spectrum Separation

The method of spectrum separation, which is illustrated in Figure 3, has the potential to address both these problems. By representing each spectrum as a linear

combination of constituent spectra one obtains a set of spectra that are applicable across different voxels. In addition, one obtains spectral images, which quantify the relative abundance of tissue types contributing to the observed spectrum in each voxel. In the proposed method constituent spectra are extracted directly from the data without the need for reference spectra.

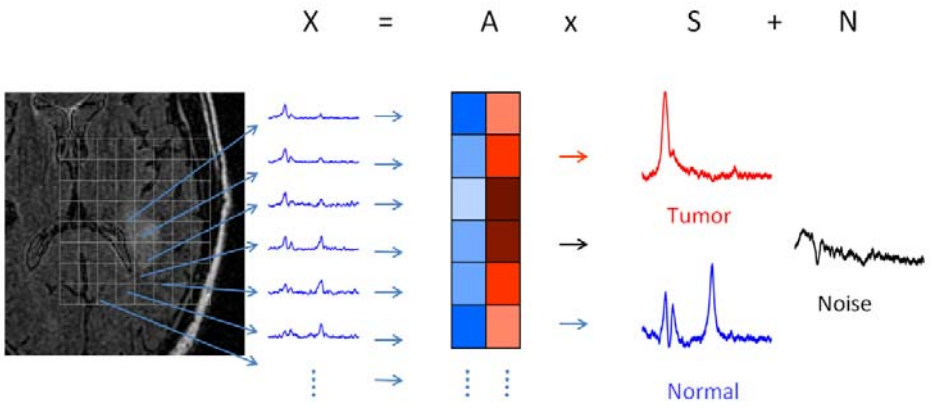

Figure 3: Sketch of spectrum separation

Spectra of multiple voxels ***X*** are simultaneously analyzed and decomposed into constituent spectra ***S*** and the corresponding abundance distributions ***A***. The constituent spectra extracted directly from the data can be identified by comparing them to known spectra of individual tissue types (normal tissue and tumor tissue in this study)

The signal measured in MRSI is the response to a coherent stimulation of the entire tissue. As a result the amplitudes of the different coherent resonators are additive and their spectral magnitudes are additive. The overall gain with which a tissue type contributes to this addition is proportional to its abundance in each voxel. As a result one can explain the observed absorption spectra arranged as a matrix ***X*** as a product of abundances ***A*** with constituent tissue spectra ***S*** and additive measurement noise ***N***:

$$\mathbf{X} = \mathbf{A}\,\mathbf{S} + \mathbf{N}, \tag{1.1}$$

The columns in matrix $\boldsymbol{A}$ represent the abundance of the constituent tissue and the rows in matrix $\boldsymbol{S}$ represent their corresponding spectra. Matrix $\boldsymbol{N}$ represents additive noise. This linear superposition holds for the absorption spectra, which are the real values of the frequency decomposition of the recorded time domain MRSI signal, i.e. the free-induction-decay (FID) or echo pulse (50). The abundance matrix $\boldsymbol{A}$ has M columns (one for each constituent) and N rows (one for each voxel). $\boldsymbol{X}$ and $\boldsymbol{S}$ have L columns (one for each resonance band). Since we interpret $\boldsymbol{A}$ as abundance, we can assume the matrix to be non-negative. In addition, since the constituent spectra, $\boldsymbol{S}$, represent amplitudes of resonances, in theory the smallest resonance amplitude is zero, corresponding to the absence of resonance at a given frequency. The factorization of Equation (1.1) is therefore constrained by,

$$\boldsymbol{A} \geq 0 \text{ and } \boldsymbol{S} \geq 0, \tag{1.2}$$

2.5 Conventional Spectral Analysis Methods

Equation (1.1) represents a linear superposition, which accurately reflects the superposition of the resonance signal under the assumption of a homogeneous field. This holds for absorption spectra, i.e. the real values of the Fourier transform of the observed free-induction-decay (51).

To perform this factorization there are two types of methods: model-based methods (52-54) and statistics-based methods (55,56). Model-based methods such as

Variable projection (VARPRO) (57) and LCModel (58) impose an explicit or parametric model on $\boldsymbol{S}$ with biochemical prior knowledge, and consider one voxel at a time. The optimal parameters and abundances are chosen such that Equation (1.1) is satisfied with the smallest possible noise $\boldsymbol{N}$. Although these model-fitting methods can quantify metabolite concentrations from the MRS data, they are also very sensitive to noise and often require assumptions on the biochemical composition of the tissue. By analyzing individual spectra, these methods fail to exploit the potential benefits of averaging that implicitly occurs when simultaneously fitting multiple spectra. Statistics-based techniques such as principal component analysis (PCA) (59-61) and independent component analysis (ICA) (61-63) instead use all spectra simultaneously to extract constituent components. Thus, they exploit the statistical structure of multi-voxel spectra to solve for all rows in Equation (1.1) simultaneously. Instead of making explicit assumptions about the structure of $\boldsymbol{S}$ these techniques assume statistical properties such as co-variation or independence. One of the problems with these earlier approaches, however, is the common assumption that constituent spectra are orthogonal as there are many cases where the constituent spectra due to overlapping peaks (e.g. lipid and lactate) can be highly correlated, and therefore an orthogonality or independence assumption is incorrect.

2.6 Nonnegative Matrix Factorization

Nonnegative Matrix Factorization (NMF) algorithm (1) is another statistics-based algorithm to perform the factorization. It is a classic blind source separation algorithm

which includes a positivity constraint but avoid the sparseness assumption. This algorithm exploits the fact that both abundances and spectra can only take on positive values. Negative values in the data are ascribed to the noise term leading to a constraint version of the NMF algorithm (cNMF). The advantage of the resulting estimation process is that no reference spectra are required. Instead, the algorithm can adapt to the heterogeneous spectra observed for different tumors. It has shown that assumption of sparseness of the constituent spectra is not necessary, and in fact may be detrimental. In this thesis, we will focus on the application of NMF on brain tumor MRSI spectral analysis.

2.7 Origins of Spectral Variability

To assess the potential benefit of spectrum separation it is useful to quantify the various effects that contribute to spectral variability. An approximate estimate can be obtained by considering for instance the effect on the CNI. The resulting numbers show that the main source of variability is the partial volume effect: a given voxel may have anywhere from 0% tumor tissue to 100%. Assuming an average CNI of 0.5 for normal tissue, and 4 for a malignant tumor (46,64), a voxel containing at fraction of tumor tissue may have a CNI anywhere between 0.5 and 4. This corresponds to a range of approximately 18dB. A second source of variability is measurement noise. In our clinical data the noise floor can be as much as 1/2 of the choline peak in normal brain tissue. This leads to a variability of up to 6dB in the CNI of normal tissue. Finally, inherent tumor heterogeneity may also lead to variable CNI. We are not aware of published results

explicitly assessing variability as result of heterogeneity (excluding partial volume and noise effects). Given that between low and high-grade tumors the CNI changes in average by a factor of 1.5-2 (46,64), it may be fair to assume 3-6dB in variability due to tumor-heterogeneity. Spectrum separation therefore aims to address the two strongest sources of variability, i.e. partial volume effect (≈18dB), and measurement noise (≈6dB).

Chapter 3 Nonnegative Matrix Factorization

3.1 Nonnegative Matrix Factorization Algorithms

Nonnegative matrix factorization (NMF) is a recent technique for dimensionality reduction and data analysis that yields a parts-based, nonnegative representation for nonnegative input data. This technique has been successfully applied in many applications, e.g. in data analysis (pattern recognition, segmentation, clustering, dimensionality reduction) (65-79), signal and image processing (blind source separation, spectra recovering) (1,80,81), language modeling, text analysis (82), music transcription (67), or neurobiology (gene separation) (83,84).

3.1.1 NMF by Lee and Seung

Early work on nonnegative matrix factorizations was performed by a Finnish group of researchers in the middle of the 1990s under the name positive matrix factorization (85,86). It became more widely known as nonnegative matrix factorization after Lee and Seung investigated the properties of the algorithm and published some simple and useful algorithms for the factorization (71,72). The basic idea of Lee and Seung's (71) NMF algorithm to solve the unmixing problem in Equation (1.1) is to construct a gradient descent over an objective function that optimizes $\boldsymbol{A}$ and $\boldsymbol{S}$ and, by

appropriately choosing gradient step sizes, to convert additive update rules to a multiplicative ones, thus non-negativity can be guaranteed given non-negative $\boldsymbol{X}$ and nonnegative initialization of $\boldsymbol{A}$ and $\boldsymbol{S}$.

For example, with $\boldsymbol{N}$ modeled as Gaussian noise (a reasonable assumption for MRSI data), one can formulate the problem of recovering $\boldsymbol{A}$ and $\boldsymbol{S}$ as a maximum likelihood estimation.

$$A_{ML}, S_{ML} = \arg\max_{A,S} p(X|A,S) = \arg\max_{A,S} \frac{1}{\sqrt{2\pi}\sigma} e^{-\frac{\|X-AS\|^2}{2\sigma^2}}$$

$$\text{Subject to: } A \geq 0,\ S \geq 0, \tag{3.1}$$

where σ is the deviation of the Gaussian noise and (AS) its mean.

Maximizing the likelihood is equivalent to minimizing the negative log-likelihood (NLL), and Equation (3.1) can be written as,

$$A_{ML}, S_{ML} = \arg\min_{A,S}(-\log p(X|A,S)) = \arg\min_{A,S}\|X-AS\|^2$$

$$\text{Subject to : } A \geq 0,\ S \geq 0, \tag{3.2}$$

Defining the negative log-likelihood as $F = \|X-AS\|^2$, the gradients of $\boldsymbol{F}$ for $\boldsymbol{A}$ and $\boldsymbol{S}$ are given by,

$$\frac{\partial F}{\partial A_{i,m}} = -2 * ((XS^T)_{i,m} - (ASS^T)_{i,m})$$

$$\frac{\partial F}{\partial S_{m,\lambda}} = -2 * ((A^T X)_{m,\lambda} - (A^T AS)_{m,\lambda})$$

where i, m and λ are indices for the matrices of ***A*** and ***S***, as i = 1 ,…, N, m = 1 ,…, M, and λ = 1,…, L.

Using the gradients we can construct the additive update rules,

$$A_{i,m} \leftarrow A_{i,m} + \delta_{i,m}\left[(XS^T)_{i,m} - (ASS^T)_{i,m}\right]$$

$$S_{m,\lambda} \leftarrow S_{m,\lambda} + \eta_{m,\lambda}\left[(A^T X)_{m,\lambda} - (A^T AS)_{m,\lambda}\right]$$

Note that there are two free parameters, which are the step sizes of the updates. Lee and Seung show that by appropriately choosing the step sizes, $\delta_{i,m} = A_{i,m} / (ASS^T)_{i,m}$, $\eta_{m,\lambda} = S_{m,\lambda} / (A^T AS)_{m,\lambda}$, the additive update rule can be formulated as a multiplicative update rule, with X = AS being a fixed point. The multiplicative update rules for ***A*** and ***S*** therefore become,

$$A_{i,m} \leftarrow A_{i,m} \frac{(XS^T)_{i,m}}{(ASS^T)_{i,m}}$$

$$S_{m,\lambda} \leftarrow S_{m,\lambda} \frac{(A^T X)_{m,\lambda}}{(A^T AS)_{m,\lambda}} \qquad (3.3)$$

This algorithm is very fast and reliable (80).

3.1.2 Variants of NMF Algorithms

Since the introduction of the NMF algorithm by Lee and Seung, a great deal of published and unpublished work has been devoted to the analysis, extension, and application of NMF algorithms in science, engineering and medicine. The NMF algorithm has been cast into alternate formulations by various authors. In general they can be divided into three general classes: multiplicative update algorithms, gradient descent algorithms, and alternating least squares algorithms. The different types of the NMF algorithms arise from using different cost functions (divergence functions) and/or by regularization of the $\boldsymbol{A}$ and/or $\boldsymbol{S}$ matrices (87).

With special consideration applying NMF algorithms to MRSI data, one problem is that, due to Gaussian noise in MRSI data, the observations $\boldsymbol{X}$ can have negative values. Since all observations are used in updating $\boldsymbol{A}$ and $\boldsymbol{S}$, non-negativity will not be guaranteed even if $\boldsymbol{A}$ and $\boldsymbol{S}$ are initialized as non-negative. This can lead to physically unrealistic solutions for the recovered spectra - i.e. spectra with negative amplitudes. Thus improvement of the NMF algorithm is necessary for MRSI data analysis to provide biochemically meaningful and physically interpretable solutions significant for analysis.

3. 2 Constrained Nonnegative Matrix Factorization (cNMF)

cNMF is a modified NMF algorithm by first adding an initialization step for the matrices, constructing a non-negative random $\boldsymbol{A}$ and estimating $\boldsymbol{S}$ by solving a non-negatively constrained least squares problem,

$$\arg\min_{A,S} \|X - AS\|^2, \quad \text{subject to } S \geq 0$$

We disallow negative spectral magnitude values and instead assume that they are due to baseline noise. This is enforced by introducing a threshold constraint on ***S***,

$$S_{m,\lambda} = \begin{cases} S_{m,\lambda} & S_{m,\lambda} > 0 \\ \varepsilon & S_{m,\lambda} \leq 0 \end{cases} \tag{3.4}$$

where ε is some very small positive value. We treat ***A*** symmetrically, using the same positivity constraint as mentioned above. This ensures ***A*** and ***S*** remain nonnegative, given the possibility of negative values in ***X***. Based on Lee and Seung's convergence proof for NMF (88), constraint (Equation (3.2)) will not change the convergence characteristics of the cNMF algorithm, although the speed of convergence may be reduced. However a least squares initialization is useful for improving the speed of convergence. An empirical demonstration of convergence for cNMF is given in (80).

To summarize, the procedure for updating ***A*** and ***S*** is:

1. Choose dimensions of ***A*** and ***S.***
2. Initialize ***A*** and ***S*** with non-negative values (random ***A*** and constrained least squares for ***S***).
3. Updates ***A***.
4. Force negative values of ***A*** to be approximately zero.
5. Update ***S***.
6. Force negative values of ***S*** to be approximately zero.
7. Iterate (back to 2) until convergence.

Chapter 4 Data Preprocessing

Human subjects in this study are part of the routine clinical patient population at Memorial Sloan-Kettering Cancer Center (MSKCC) with pathologically proven brain gliomas (the most common primary brain tumors representing 39% of all brain tumors and 81% of all malignant tumors (89)). Since the clinical used GE spectrum analysis software (Functool) does not output the computed spectra numerically. For our analysis it was therefore necessary to redevelop the corresponding data conditioning routines starting with the raw time-domain data (GE P-files).

4.1 Human Subjects

Thirty-two patients were evaluated in the study. Of these, we selected 20 MRSI scans with sufficient data quality. Among the 20 patients (all of whom had received some form of treatment prior to the scan), 10 were low-grade (WHO grade I-II) gliomas (LGG) including WHO grade II astrocytoma, oligodendrioglioma, and oligoastrocytoma, and the other 10 were high-grade (WHO grade III-IV) gliomas (HGG) including anaplastic astrocytoma, anaplastic oligodendrioglioma, and glioblastoma. This categorization was used as truth data for the classification. Institutional Review Board (IRB) waiver was obtained to retrospectively analyze clinical proton MRSI data and examine the medical records.

4.2 Data Acquisition

This study analyzed MRSI and MRI scans following the routine clinical protocol for brain tumor patients at MSKCC. The MRSI data were collected using a long echo time (TE=144ms, TR=1000ms) 3D PRESS sequence with water suppression (PRESS box is shown as white box in Figures 2, 8, 12, 15 and 16). The 1.5 Tesla GE Scanner (General Electric Medical Systems, Milwaukee, WI) enable us to acquire data with MRSI voxel size ranging from 1 cm^3 down to 0.5^3 cm^3. The acquisition or phase encoding volume typically covers 8x8x8 voxels at $1cm^3$ per voxel. FLAIR, T2, and T1 post-contrast MRI were collected in alignment to the MRSI study so that they can be combined for diagnosis and tumor segmentation as shown in Figures 2, 8, 12, 15, or 16. Prior to MRSI acquisition, 3 mm thick FLAIR scout images were collected for prescribing MRSI acquisition. The PRESS excitation volume encompassed the areas of FLAIR imaging abnormalities, as well as ample normal appearing brain tissue in the surrounding region. For some exceeding large tumors, the MRSI field of view (FOV) may need to be increased to 10-12 cm to accommodate large PRESS excitation volume, resulting in nominal MRSI voxel size of 1.6-2.2 cc. If the tumor is located well beneath the skull and the resultant rectangular PRESS excitation volume does not include any skull fat, outer-volume-saturation (OVS) RF pulses will not be employed. For those tumor located adjacent to the skull, however, OVS pulses will be applied to reduce signal contamination caused by the skull fat lipids. Raw time-domain MRSI data and FLAIR images were exported anonymously for data processing. MSKCC provided the final diagnosis as truth data for the classification after a full diagnostic workup for all subjects.

4.3 Data Preprocessing

The data preprocessing routines, written in MATLAB, filtered residual water signal, performed phase correction, and corrected for frequency shifts due to an inhomogeneous magnetic field. The results of this processing are equivalent to those obtained with Functool.

Water Filtering

The most critical step in preprocessing is to remove the low frequency signals due to water, which tend to overwhelm, in particular, Cho and Cr spectral lines. We used a 3rd order Butterworth high-pass filter with 75Hz cutoff applied forward and backward in time to avoid phase distortions (MATLAB filtfilt function).

Zero Filling

The time domain FID data typically contains 512 samples at 1 kHz sampling frequency. To increase spectral resolution, we increased the length of the signal by appending zero values to a length of 1024.

Line Broadening

To reduce the effect of noise one can smooth the spectrum by windowing the data in the time domain. We used exponential windowing resulting in a 3Hz line broadening, which compromises between noise and resolution.

Frequency Decomposition

After these steps the frequency-domain data were recovered from the 3D phase encoded FID time-domain sequences with a 4D Fourier transform. The only remaining

step that has to be validated is a potential phase encoding offset, which would manifest itself in a spatial misalignment of the spectra with the FLAIR images.

Phase Correction

Phase distortions are particularly problematic, as they will lead to negative values in the absorption spectra violating the main assumption of the NMF algorithm. More importantly, if the phase is not corrected to give the same effective phases across voxels, the assumption that the constituent spectra are the same across voxels is violated. To ensure positive spectra one has to determine for each voxel a separate phase factor. The noise levels and phase distortions due to an inhomogeneous field are significant in these clinical data. Moreover, at long TE values an inverted lipid/ lactate peak at 1.3 ppm may be present with a 180^{o} degree phase that cannot be corrected. So instead of the conventional zero and first order phase correction, we opted to use the absolute value of the spectrum rather than the real (absorption) spectrum.

Frequency Alignment

The spectrum separation method operates simultaneously on multiple spectra and assumes that the constituent spectra coincide across voxels. To determine potential frequency shifts, we cross-correlated the resulting absolute spectra and adjusted frequency shifts individually for each voxel by no more than 0.3ppm to maximize correlation in the frequency range of 1.6 – 3.6ppm. This method worked well on the present data with SNR>4dB. Baseline correction or modeling was not required.

The MRSI data were preprocessed automatically and identically for all data sets. This resulted for each patient scan in 8×8×8 (N = 29) or 16x8x8 (N = 3) spectra with 1024 points covering 1 KHz spectral width.

Proper preprocessing of the MRSI data is essential for successful spectral analysis. Particularly in this study, with application of the spectrum separation approach, the significant phase and frequency variations among spectra can be particularly problematic because of violation of the assumption that the constituent spectra are the same across voxels. These phase encoding artifacts may arise from the instrumental imperfections, field inhomogeneity, patient movement, etc. Details of the phase encoding offsets will be discussed in the following chapter through a theoretical study.

Chapter 5 Theoretical Study of the Phase Encoding Artifacts

As discussed in the previous chapter, the phase encoding artifacts especially the phase distortions are significant in the clinical data and the conventional zero and first order phase correction is not sufficient to correct the phase errors. The phase distortions may lead to negative values in absorption spectra, which violates the main assumption of the NMF algorithm. Another assumption of spectrum separation approach is that the constituent spectra are the same across voxels. This assumption is violated if the phase distortions are not corrected to give the same effective phases across voxels. In addition, the frequency distortions leading to variations in peak positions will further violate this assumption. In the following section the possible phase encoding artifacts will be discussed in details and a theoretical model is proposed to investigate how the most common phase distortions propagate into NMR data.

5.1 Phase Distortions

Phase distortions in MRSI usually result from equipment settings (the difference between frequencies of transmitter and receiver) and delay between emission of the excitation pulse and registration of the signal during the registration the FID. In particular, the sources of the phase error involved in NMR imaging include (a) misadjustment of the reference phase relative to the receiver phase detector, (b) the hardware filter network

used for noise reduction and other types of electronic filters, (c) mismatch of the acquisition onset time, (d) finite length of pulses and introduction of non-uniform distribution of transverse magnetization components across the slice due to imperfect selective radiofrequency pulses, and (e) amplifier dead time.

In addition, the variation in the B_0 homogeneity which leads to the non-uniform field fluctuations across voxels can cause further phase distortions due to the spatial variation in the Larmor frequency. Also, most MRI techniques acquire FID's in the presence of externally imposed field gradients (B_1). Since the gradient-generating circuitry cannot be completely noise free, it gives rise to spatially correlated fluctuations of the generated linear gradients. Consequently, there exists a distribution of signal contributions arising from those. The exact form of the distribution is rather complicated and closely interwoven with the image itself, indicating that it leads to patterned image artifacts rather than to a simple, uniform loss of resolution. Precise shimming can minimize the effect of B_0 and B_1 inhomogeneity, however, in 2D and 3D spectroscopic imaging experiments a uniform magnetic field throughout the whole of the volume of interest (VOI) is difficult to attain.

An example of the original spectra with the phase encoding artifacts is shown as blue curve in Figure 4a. Clearly, the original spectrum shows significant phase errors which are reflected in the distorted signals with peaks pointing down and appearing to be negative. The phase encoding artifacts also lead to frequency shifts as shown in the green line (spectrum before frequency alignment) compared to red curve (spectrum after frequency alignment) in Figure 4a.

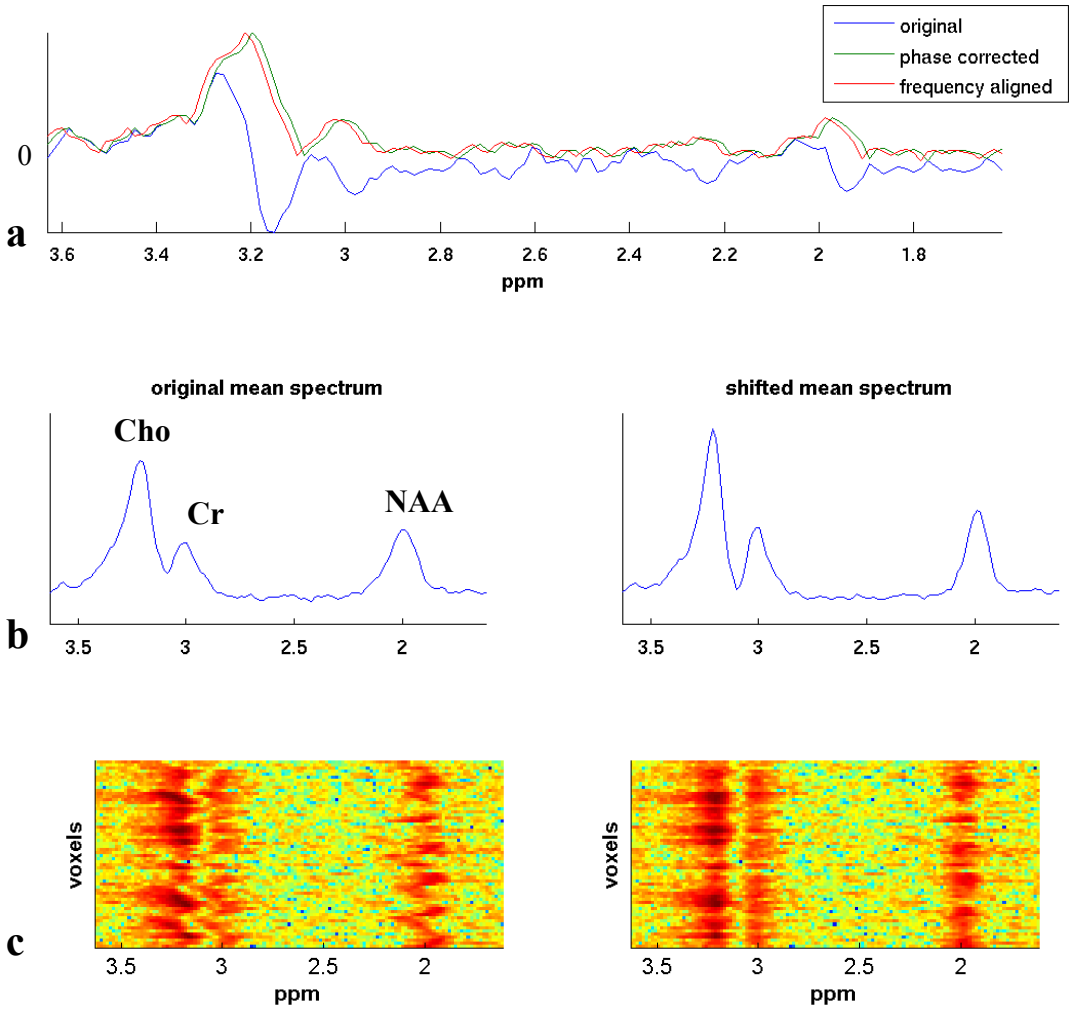

Figure 4: Example of phase correction and frequency alignment

4a: Example spectrum before and after phase correction and frequency alignment. The original spectrum in blue line shows significant phase errors. The distortion leads to the peak signals pointing down and appearing to be negative. Green curve shows the spectrum after the phase correction (absolute spectrum) and the red curve shows the spectrum after the frequency alignment which is done here by cross-correlating the absolute spectrum and adjusting frequency shifts to maximize correlation to the mean spectra. **4b**: Mean spectra across voxels before and after the frequency alignments. The original mean spectra show overlapped Cho and Cr peaks due to the spectral frequency shifts among voxels. **4c**: Spectral intensity maps before and after frequency alignments. Horizontal axis is chemical shift in part per million (ppm) and vertical axis represents different voxels. Color indicates spectral intensity in each of the frequency band with red indicating high intensity and blue indicating low intensity.

The spectral distortions introduced by the phase encoding artifacts make phase and frequency correction a universal problem in phase-sensitive Fourier transform nuclear magnetic resonance experiments. For our clinical data, we are able to sufficiently align the spectra by cross-correlating the absolute spectra to the mean spectrum across all the voxels, but the traditional 0^{th} and 1^{st} order phase correction is not sufficient to obtain real absorption spectra. As a result we instead use the absolute spectrum to ensure the accuracy of the subsequent spectrum separation analysis. This operation fulfils positivity requirement of the NMF algorithm but it introduces a non-linear distortion to the system which violates the linear model assumption. The ultimate goal is to use real spectrum to perform the decomposition. Therefore a robust phase correction algorithm is needed.

In the following section, we performed a theoretical analysis to dissect how the phase encoding artifacts propagate into NMR. In the analysis, two of the most common distortions - the delay of registration the FID (equipment setting error) and spatial magnetic field fluctuations (magnetic field inhomogeneity) – were incorporated into the theoretical model with the intension to improve the current phase correction algorithm.

5.2 Theoretical Study

For simplicity, we consider a 2D (1D spatial 1D spectral) CSI signal example for the effect of field inhomogeneity and time delays. Assume an effective magnetic field,

$$\tilde{B}_0(x) = B_0 - \Delta B(x) \tag{5.1}$$

where B_0 is the dominating space-independent field and $\Delta B(x)$ is the magnetic field inhomogeneity at the point x. The delay of registration of the FID (the delay between the end of the last pulse and the start of acquisition of the echo signal) is represented as t_0. In the presence of these two distortions, the signal induced in the RF coil can be expressed as:

$$S_r(G_x,t)=\iint dx\,d\sigma\rho(x,\sigma)e^{-i\gamma(1-\sigma)\tilde{B}_0(t+t_0)}e^{-i\gamma(\tilde{B}_0+G_x x)(1-\sigma)\tau} \tag{5.2}$$

where $\rho(x,\sigma)$ is the spectroscopic spin density at point (x,σ); σ is the chemical shift expressed in parts per million (ppm) and characterizes the chemical environment of the nuclei. It quantifies the change of the effective magnetic field of each nuclei as a results of the rotation of the spin associated with the nuclei in the magnetic fields. The effective field is still proportional to the applied magnetic field B_0 but varies among different protons in a metabolite. This leads to a shift in resonance frequency which refer to chemical shift; γ is the gyromagnetic ratio in rad s^{-1} mT^{-1}; G_x is the linear magnetic phase-encoding gradient having units of mT m^{-1}; $\tilde{B}_0$ denotes main magnetic field with distortions as defined in Equation (5.1). In the following section of theoretical deduction, $\tilde{B}_0$ and ΔB will be used instead of $\tilde{B}_0(x)$ and $\Delta B(x)$ to simplify the notation.

$S_r(G_x,t)$ in the Equation (5.2) represents the total 2D FID signals emitted as a function of time for each applied phase-encoding gradient. The signal detected is generated by all metabolites in the entire sample, therefore one has to integrate over space and chemical shift to obtain the total radiation emitted by the entire sample. The strength of the resonance signal emitted at position x and chemical shift σ is proportional

to spin density ρ. Hence spin resonances at $\gamma(1-\sigma)\tilde{B}_0$ and the oscillation is captured at $e^{-i\gamma(1-\sigma)\tilde{B}_0(t+t_0)}$ with corresponding delay of t_0. However the precise phase will depend also on the excitation sequence during time τ and proportional to the effective magnetic field at location x which is given as $\gamma(\tilde{B}_0+G_x x)(1-\sigma)\tau$. A point in the image space $S_r(G_x,t)$ is a function of time and applied phase-encoding gradient with frequency in the time coordinated representing chemical shift and frequency of gradient coordinate linking to space. Thus after Fourier transform over time and applied gradient, one obtain the spectral image as a function of space and chemical shift. Taken together, the goal of in magnetic field spectroscopy is to find the relative amplitudes of the different frequency components and the spatial information of the signals of different tissue components $\rho(x,\sigma)$.

Hence, the purpose of the follow analysis is to find the link between the spectroscopic spin density in the presence of the introduced distortions and the actual $\rho(x,\sigma)$.

Expanding the Equation (5.2) we get:

$$S_r(G_x,t)=\iint dx\,d\sigma\rho(x,\sigma)e^{-i\gamma[B_0(t+t_0+\tau)-B_0\sigma(t+t_0+\tau)-\Delta B(t+t_0+\tau)+\Delta B\sigma(t+t_0+\tau)]}e^{-i\gamma(G_x x\tau-G_x x\sigma\tau)} \quad (5.3)$$

The emitted signal $S_r(G_x,t)$ is not used directly. In practice the signal is demodulated by multiply e^{iw_0} if the w_0 is chosen to be γB_0. After removal of the carrier frequency ω_0 from the signal, the demodulated signal can be written as:

$$S(G_x,t) = e^{iw_0} S_r(G_x,t)$$
$$= \iint dx\, d\sigma \rho(x,\sigma) e^{-i\gamma[B_0(t_0+\tau)-B_0\sigma(t+t_0+\tau)-\Delta B(t+t_0+\tau)+\Delta B\sigma(t+t_0+\tau)]} e^{-i\gamma(G_x x\tau - G_x x\sigma\tau)} \tag{5.4}$$

Since σ is generally less than or on the order of 10^{-5} (90) and as a result the term $\gamma G_x x\sigma\tau$ is much less than 2π (phase), it is therefore valid to simplify the equation by ignoring this term and the approximate equality of Equation (5.4) becomes:

$$S(G_x,t) \approx \iint dx\, d\sigma \rho(x,\sigma) e^{-i\gamma[(B_0-\Delta B)(\tau+t_0)-(B_0-\Delta B)\sigma(t_0+\tau)]} e^{i\gamma(\Delta B+B_0\sigma-\Delta B\sigma)t} e^{-i\gamma G_x x\tau} \tag{5.5}$$

Let $\bar{\gamma} = \gamma/2\pi$, and Equation (5.5) cab be rewritten as:

$$S(G_x,t) \approx \iint dx\, d\sigma \rho(x,\sigma) e^{-i2\pi\bar{\gamma}[(B_0-\Delta B)(\tau+t_0)-(B_0-\Delta B)\sigma(t_0+\tau)]} e^{2\pi\bar{\gamma}(\Delta B+B_0\sigma-\Delta B\sigma)t} e^{-i2\pi\bar{\gamma}G_x x\tau} \tag{5.6}$$

To establish the precise relationship between the original species profile (spectrum), $\rho(x,\sigma)$ and the one obtained in the present of introduced distortions, we now apply the 2D Fourier transform of $S(G_x,t)$:

$$s(u,v) = 2DFT[S(G_x,t)]$$
$$= \iint dx\, d\sigma \rho(x,\sigma) e^{-i2\pi\bar{\gamma}[(B_0-\Delta B)(\tau+t_0)-(B_0-\Delta B)\sigma(\tau+t_0)]} \iint dG_x\, dt e^{i2\pi\bar{\gamma}(\Delta B+B_0\sigma-\Delta B\sigma)t} e^{-i2\pi\bar{\gamma}G_x x\tau} e^{-i2\pi\bar{\gamma}(vtB_0-uG_x\tau)}$$
$$= \iint dx\, d\sigma \rho(x,\sigma) e^{-i2\pi\bar{\gamma}[(B_0-\Delta B)(\tau+t_0)-(B_0-\Delta B)\sigma(\tau+t_0)]} \int dG_x e^{i2\pi G_x(\bar{\gamma}u\tau-\bar{\gamma}x\tau)} \int dt e^{i2\pi t(\bar{\gamma}\Delta B+\bar{\gamma}B_0\sigma-\bar{\gamma}\Delta B\sigma-\bar{\gamma}B_0 v)}$$
$$= \iint dx\, d\sigma \rho(x,\sigma) e^{-i2\pi\bar{\gamma}[(B_0-\Delta B)(\tau+t_0)-(B_0-\Delta B)\sigma(\tau+t_0)]} \delta(\bar{\gamma}u\tau - \bar{\gamma}x\tau)\delta(\bar{\gamma}\Delta B + \bar{\gamma}B_0\sigma - \bar{\gamma}\Delta B\sigma - \bar{\gamma}B_0 v) \tag{5.6}$$

According to the sifting property of the delta function, the above signal expression of Equation (5.6) is sifted out at:

$$x = u \qquad \sigma = \frac{v-\Delta B/B_0}{1-\Delta B/B_0} \tag{5.7}$$

With the result in Equation (5.7), the 2D Fourier transform of the observed FID signal becomes proportional to:

$$s(u,v) \propto \rho(u, \frac{v-\Delta B/B_0}{1-\Delta B/B_0}) e^{-i2\pi\bar{\gamma}(B_0-\Delta B)(\tau+t_0)} e^{i2\pi\bar{\gamma}(B_0-\Delta B)\frac{v-\Delta B/B_0}{1-\Delta B/B_0}(\tau+t_0)}$$
$$\propto \rho(u, \frac{v-\Delta B/B_0}{1-\Delta B/B_0}) e^{-i2\pi\bar{\gamma}B_0(\tau+t_0)} e^{i2\pi\bar{\gamma}v(\tau+t_0)} \quad (5.8)$$

After moving the 0th and 1st order phase distortion terms to the left hand side of the Equation (5.8), the reconstructed spectral image ρ in the presence of magnetic field distortions ΔB and equipment setting errors t_0 can be written as:

$$\rho(u, \frac{v-\Delta B/B_0}{1-\Delta B/B_0}) \propto s(u,v) e^{i2\pi\bar{\gamma}B_0(\tau+t_0)} e^{-i2\pi\bar{\gamma}v(\tau+t_0)} \quad (5.9)$$

As shown in above equation (5.9), both phase and frequency distortions exist in the observed spectra. The distortion terms are a function of the introduced distortions of field inhomogeneity ΔB and time delays t_0. In order to recover the original spectral profiles, the spectra profiles obtained after 2D Fourier transform *s(u,v)* need to be corrected accordingly. In the following section, we will discuss in details about the observed modification of the spectra in the presence of the field inhomogeneity and time delays as well as the method used to correct the distortions.

5.3 Modified Spectrum in the Present of Field Distortions

From the above equation, clearly there are two distortion terms modifying the spectra:

1. Phase modification term $e^{i2\pi\bar{\gamma}B_0(\tau+t_0)} e^{-i2\pi\bar{\gamma}v(\tau+t_0)}$

These two terms lead to the zero-order and first order phase errors. The analysis indicates that both errors are global, meaning there is a same phase factor across the

whole volume. The 0^{th} and 1^{st} order phase corrections are routine procedure for MRSI studies.

2. Frequency modification term $\frac{v-\Delta B/B_0}{1\ \ \Delta B/B_0}$

This term of distortion leads to both shifting and stretching of the spectra. In routine preprocessing, frequency alignment is done by only correcting the frequency shift term but the stretching term is usually ignored.

Interestingly, according to the above analysis the field distortions (ΔB) do not introduce phase errors but instead lead to frequency shifting and stretching. The main phase errors are introduced by t_0, i.e. the delay of registration of the FID. It means in this proposed theoretical model phase can be corrected globally. But of course in the real situation there are other phase errors involved in NMR imaging such as environment noise, sample motion and systematic variations. For the clinical data, there might be further distortion and artifact introduced by certain structure or certain diseases. It is known that regions such as the sinuses and necrotic tissue are likely to cause large variations in susceptibility. Therefore in routine spectral preprocessing, phase correction is usually performed locally (voxel by voxel).

Also, the theoretical analysis suggests that the frequency alignment should be done by not only shifting but also stretching the spectra ($\frac{v-\Delta B/B_0}{1-\Delta B/B_0}$). The analysis also indicted that the frequency shift and stretch actually have the same factor ($\Delta B/B_0$). This is a quite distinct approach for frequency alignment not discussed in published literature.

Routinely frequency alignment is performed by only shifting the data according to the reference spectra (in our case the averaged spectra across the whole volume as shown in Figure 4b and 4c) but ignoring stretching the spectra. There are several possible reasons for this. For an example, the actual frequency shift for the clinical data is quite small (~0.03ppm), therefore to perform frequency alignment by simply shifting the spectrum is sufficient for the clinical MRSI data. Also, this small stretching will not help much in improving phase correction. On the other hand, stretching the spectra will lead to certain degree of spectra broadening which usually adversely affect spectral analysis. However, our analysis indicates that for data with significant frequency shifting errors, one could stretch the spectra concurrently with frequency shifting to get better aligned spectra.

From the theoretical analysis, we now have a better idea about how the introduced distortions propagate in to the spectra. And also based on the final modified spectrum we have a better understanding of the logic behind each preprocess procedure in the frequency domain spectral analysis. Unfortunately the analysis does not help in fixing the phase problem. Phase correction has always been a challenge in the spectrum analysis. It is well known that there are many possible distortions affecting the obtained spectra. In addition to the most common artifacts mentioned above, variations of magnetic susceptibility, areas of necrosis and edema etc. will lead to further phase errors.

In the following chapters of this thesis, all spectrum separation results are from absolute spectra. Although using absolute values of the spectral ensures the positivity, it introduces non-linear distortions to the system. The effects of using absolute spectra and thus violating the linear model will be discussed in the following chapter.

Chapter 6 Linearity Validation and Data Quality

Compared to a previous research study (1) the clinical scans of this study are characterized by significant background noise, phase distortions, and frequency shifts indicating field inhomogeneities. For this data we developed data conditioning routines to ensure proper filtering of residual water signal, as well as correcting for frequency shifts due to an inhomogeneous magnetic field. Phase correction proved difficult due to significant noise in the data. We opted therefore to operate on absolute spectra rather than the real-valued absorption spectra. While this guaranteed positive spectra and resolved potential inconsistencies across voxels it did introduce a non-linear distortion as a result of the absolute value operation. Fortunately, taking the absolute value of a sum of complex numbers is approximately a linear operation if the sum is dominated by a single element. Here, this means that linearity of the model may be approximately preserved if the resonance lines do not overlap and the noise is small. This is also true for 180^{o} degree inverted peaks such as lactate.

To confirm whether the linear model is sufficient in the present context, we compared, using the simulated data, the absolute spectra obtained for mixed voxels to the sum of the absolute spectra of pure voxels.

6.1 Simulated Data for Linearity Validation

Non-linear distortions originating from an inhomogeneous field and the use of absolute spectra may lead to a violation of the linear model of Equation (1.1). Thus we tested the validity of the linear model assumption on simulated data (53,91). Idealized FID sequences were generated in the time domain ($N = 512$) as the sum of $K = 3$ exponentially damped complex sinusoids which corresponded to the specific resonances peaks for H_2O, NAA and Cho:

$$s_n = \sum_{k=1}^{K} \alpha_k e^{i\varphi_k} e^{(-d_k + i2\pi f_k) t_n} \quad , \; n = 1,..., N$$

where s_n represents the n-th data point of the simulated signal; $\boldsymbol{i}$ represents the imaginary unit; the parameters α_k, φ_k, d_k, and f_k denote the amplitude, phase, damping factor, and frequency, respectively; and $t_n = n\Delta t$, with the sampling interval Δt.

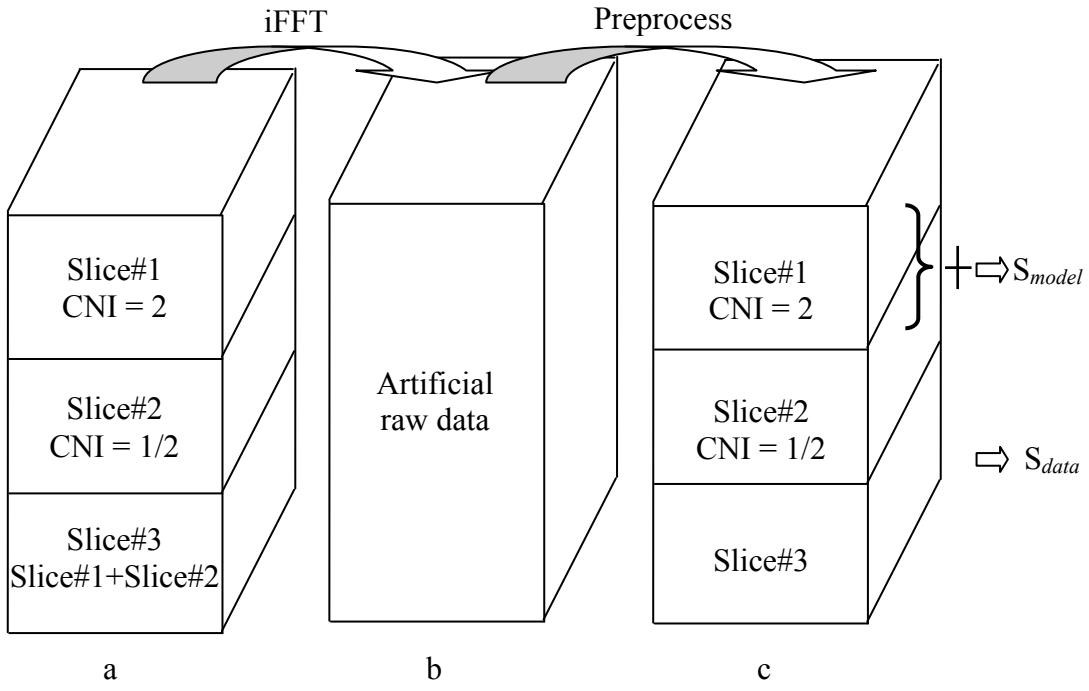

Figure 5: A schematic overview of the linearity validation on the artificial data

5a shows 3 slices of 8 by 8 artificial frequency domain data with one slice corresponding to a CNI of 2, a second slice to a CNI of 1/2, and the third mixed slice generated by adding the first two slices together. **5b** shows the corresponding time domain raw data with adding phase and frequency distortions and various levels of additive Gaussian-distributed white noise. **5c** shows the resulted spectra data after applying the same preprocessing algorithms used for the clinical data. A linear model denoted as S_{model} is generated by adding the spectra from the first two slices together and compared with the mixed spectra S_{data} from the third slice.

As demonstrated in Figure 5, three 8x8 slices of simulated MRSI data containing H_2O, NAA and Cho were generated. One slice has an Cho/NAA ratio of 2, the second one has an Cho/NAA ratio of 1/2, and the third represents a mixed spectra generated by adding the first two slices together. In order to mimic the real situation, uniform-distributed phase shifts ($\pm\pi$) and frequency shifts (±5Hz, one linewidth) were introduced variably from voxel to voxel when generating the time domain data. This is comparable to previous simulation studies which used phase shifts in the range of $\pi/4$ to $\pi/3$ and frequency shifts of 1/2 to 2 linewidth (92,93). Various levels of additive Gaussian-distributed white noise were introduced to evaluate the robustness of the preprocessing algorithm and resulting non-linearity as a function of SNR. Applying the inverse Fast Fourier Transform (iFFT) brings the frequency data to the time domain. We applied to this simulated data the same preprocessing algorithms used on the clinical data. After preprocessing, the spectra from the first two slices were added together (assuming a linear model we denote this S_{model}) and compared with the spectra from the third slice (which was generated directly from a mixed spectra, hence we call this S_{data}). The R^2 value was used to measure how well the linear addition model fits the mixed data. It is defined here as $R^2 = 1 - \sum (S_{data} - S_{model})^2 / \sum S_{data}^2$. For each SNR level, R^2 from 100 repetitions were used to assess the mean and 95% confidence intervals.

6.2 Linearity Validation

Figure 6 shows the result of the simulation for various signal-to-noise ratios. SNR was defined here as the power in the frequency range 1.8-2.2 ppm and 2.7-3.4 ppm over power in the range 0.6-1 ppm and 3.5-3.8 ppm (note that residual water will contribute to the noise estimate). These ranges have been chosen to capture the Cho, Cr and NAA signals. The black dots and the shades represent the mean R^2 value and 95% confident intervals at each SNR level. The graph indicates that the accuracy of the model depends on the noise levels. With poor SNR the linearity assumption is violated and the estimation for $\boldsymbol{A}$ and $\boldsymbol{S}$ may no longer be reliable. We measured the SNR also on our clinical data and found that the useful scans have an SNR of 4dB or higher. For those SNR values the linear model is a reasonable approximation with mean $R^2 = 0.85$. Hence, the linear model may be appropriate for the absolute spectra in a subset of clinical data with SNR above 4dB.

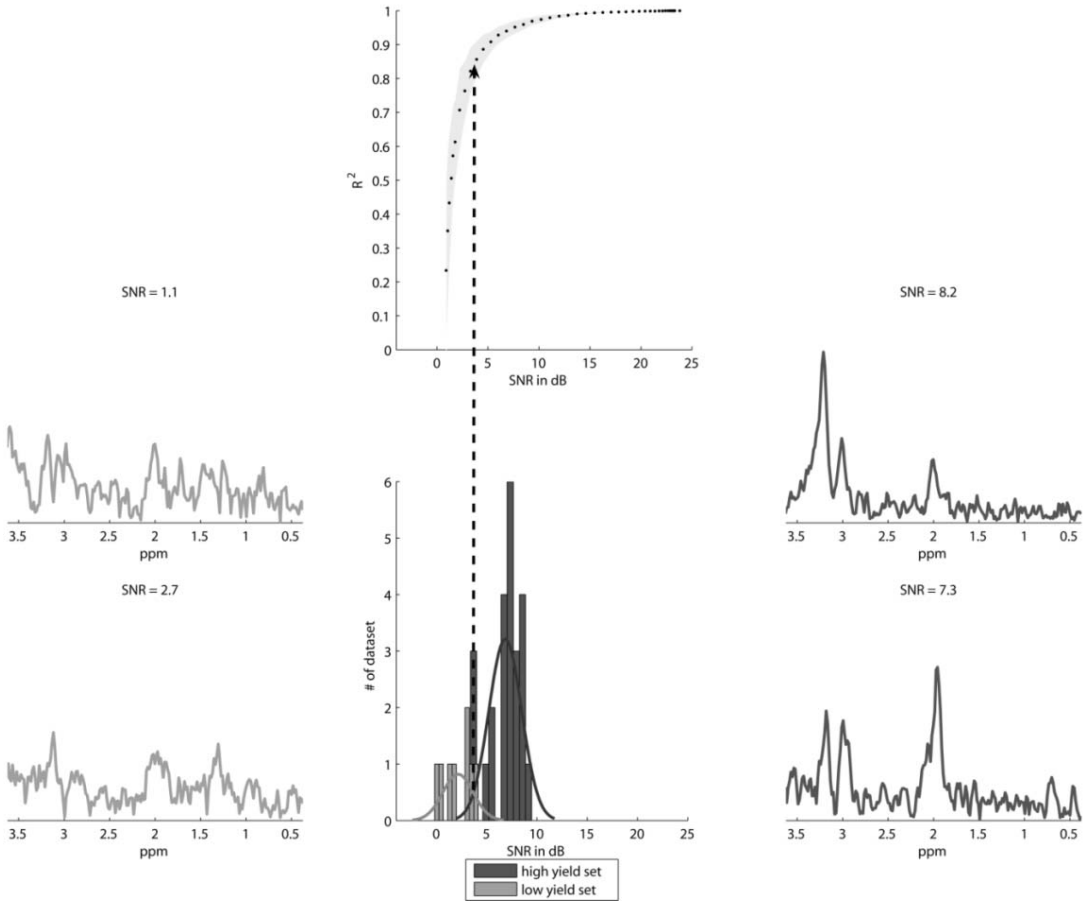

Figure 6: Linearity validation

Top graph in the center panel shows the fit of the linear model to simulated data for varying noise levels. Accuracy is measured as R^2 value capturing how well the linear model approximates the data (R^2=1 corresponds to a perfect match). Black dots represent the mean R^2 from multiple repeats (N=100) with random noise. Shading around the dots are the 95% confidence intervals. Bottom graph in the center panel shows the distribution of data quality for the 32 available clinical data sets. The data sets are divided in two groups depending on the number of useful voxels, i.e. 24 datasets with a "high yield" of useful voxels (4 datasets with radiation necrosis were excluded for further analysis) and 8 with a "low yield" of voxels. Evidently these two data sets also differ in SNR. In particular, all useful datasets have an SNR above 4dB suggesting that the linear model may be sufficient with mean R^2 = 0.85. The "low yield" data sets were excluded from the current study. Left panel shows two examples of spectra from "low yield" datasets with SNR below 4dB. Right panel shows two examples of spectra from "high yield" datasets with SNR above 4dB.

6.3 Data Quality Control

From the above simulation study, it is clear that in order to hold the linear model for the absolute spectra the MRSI data requires to have SNR above 4dB. Therefore, careful selecting data with sufficient quality is needed prior to further analysis. In addition, the specific selection of voxels will also affect the results of spectrum separation using the NMF algorithm. In particular, inclusion of noisy or distorted spectra (due to poor shimming) has a detrimental effect.

In this study, we selected rectangular volumes within the excitation box. Only slices (horizontal, coronal, sagittal) which included obvious metabolite resonance peaks in the affected brain area were selected. Peak height had to be 4dB above background for at least one voxel in the slice within the frequency ranges covering Cho (3.34–3.14ppm), Cr (3.14–2.94ppm) and NAA (2.22–1.82ppm). Examples of spectra that would have been included or excluded are shown in Figure 6. Excluded were also slices which intersected the skull with obvious distortions or lipid content. Since the algorithm we used requires multiple voxels to extract meaningful spectra we only used those "high yield" datasets with at least 10% of voxels satisfying the above criteria. Of the 32 datasets, 4 datasets with radiation necrosis and 8 "low yield" datasets were excluded, which resulted in 20 datasets for further analysis. Examples of the datasets with selected voxels are shown as colored areas in Figure 8 (excitation box delineated in white).

Chapter 7 Application of NMF on Brain Tumor MRSI

The algorithm of spectrum separation outlined in Chapter 2 and Chapter 3 decomposes the observed spectra $\boldsymbol{X}$ into constituent spectra $\boldsymbol{S}$ and associated abundances $\boldsymbol{A}$ (see also Figure 3). In this chapter we apply the NMF on brain tumor ^{1}H MRSI data to demonstrate its ability to simultaneously recover underlying source spectral patterns and their spatial concentration distributions.

7.1 Spectrum Separation by Nonnegative Matrix Factorization

The proposed model of Equation (1.1) interprets matrix $\boldsymbol{A}$ as abundance, which, therefore, only takes on non-negative values. In addition, since the constituent spectra, $\boldsymbol{S}$, represent amplitudes of resonances, in theory the smallest resonance amplitude is zero, corresponding to the absence of resonance at a given frequency. The factorization of Equation (1.1) is therefore constrained by, $\boldsymbol{A} \geq 0$ and $\boldsymbol{S} \geq 0$. The basic idea of the NMF algorithm is to maximize the likelihood for observing $\boldsymbol{X}$ given non-negative $\boldsymbol{A}$ and $\boldsymbol{S}$. Assuming Gaussian noise $\boldsymbol{N}$ the log-likelihood is simply a quadratic function which is to be maximized with respect to $\boldsymbol{A}$ and $\boldsymbol{S}$ subject to the positivity constraint. A corresponding gradient ascent algorithm is converted into a multiplicative update algorithm by appropriately choosing gradient step sizes (1,94). After preprocessing, the

absolute spectra were analyzed using the NMF algorithm (1). This process extracts spectra directly from the data, and hence no reference spectra are required. The only model parameter of NMF that needs to be determined is the dimensionality of the matrices $\boldsymbol{A}$ and $\boldsymbol{S}$, namely the number of constituent spectra to recover (i.e. M). The factorization includes an explicit subspace reduction from N dimensional space into a constrained M dimensional space, where N >>M, having the subspace capture statistical regularities in the data. Thus, choosing appropriate number of underlying sources is critical in the algorithm. In practice, there is a need to estimate as few underlying sources as possible, making the problem a low-rank approximation.

Conventional subspace analysis principal component analysis (PCA) (95) was used to determine the number of constituents. PCA involves a mathematical procedure that transforms a number of possibly correlated variables into a smaller number of uncorrelated variables called principal components. It is a way of identifying patterns in data, and expressing the data in such a way as to highlight their similarities and differences. The basic idea of PCA is to find a set of mutually orthogonal components that explain the maximum amount of variance of the data. Therefore the first principal component accounts for as much of the variability in the data as possible, and each succeeding component accounts for as much of the remaining variability as possible.

Figure 7 shows an example of PCA scree plot from one dataset with sufficient SNR. A scee plot is a plot which displays the magnitude of the eigenvalues on a line chart, to show the rate of decay of the eigenvalues. The figure shows that the slope that represents the change in the magnitude of the eigenvalues changes from very steep in the

first two eigenvalues to very shallow in the third. It is easy to see that we need only two eigenvalues to preserve most of the variance suggesting 2 constituent sources for this given example.

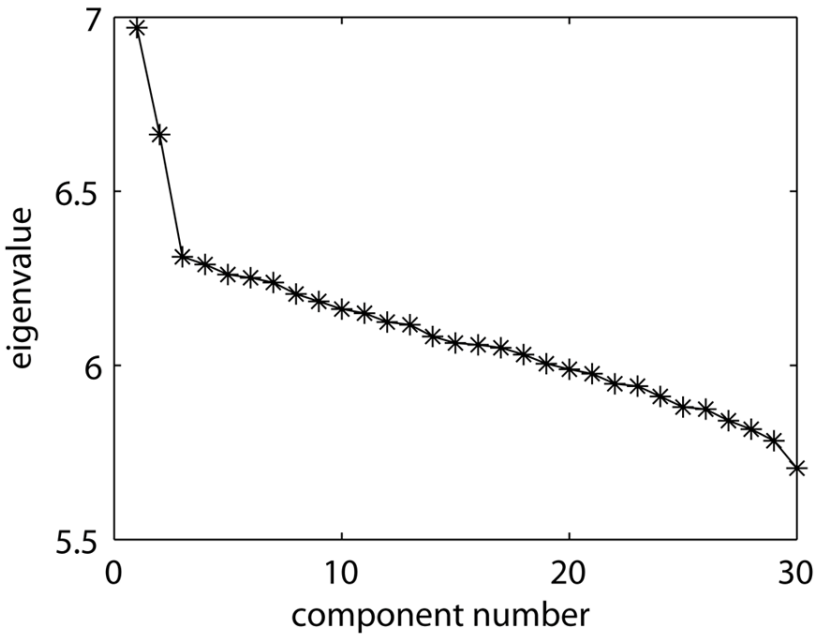

Figure 7: Estimating the number of sources by PCA scree plot

PCA scree plot was showed in log scale and sorted in descending. The result suggests that PCA estimate number of sources as 2.

7.2 Color Overlay of Tumor Abundance Map on FLAIR Image

7.2.1 Overlay Construction

To present the result of the NMF separation algorithm, we merged the FLAIR image intensity with the abundance estimates $\boldsymbol{A}$ encoded in color. Examples of this

visualization method are shown in Figure 8 and are compared to the conventional spectral display. In this overlay, the abundance of the tumor spectrum for a given voxel is represented as a color between blue (no tumor) and red (tumor). Color saturation shows how well the spectrum $\boldsymbol{X}$ is represented by the two constituents $\boldsymbol{S}$ (measured as goodness of fit, $0 \leq r^2 \leq 1$, with $r^2 = 1 - \Sigma(X - AS)^2 / \Sigma X^2$), and is hence an indirect indication for SNR. Color therefore is only visible in the region of interest inside the signal acquisition volume (white PRESS box). Brightness represents FLAIR intensity as in a conventional MRI image.

7.2.2 Result of Spectrum Separation of Clinical MRSI of Brain Tumor

The NMF separation algorithm computes the abundance of each tissue type for each voxel. This information can be used to assess the spatial extent and infiltration of the tumor beyond the intensity enhancement region. Figure 8 shows three examples of the constructed overlays from two patients with high-grade glioma (top two rows) and one patient with low-grade glioma (bottom row). The figure indicates that the two extracted spectral profiles coincide with the standard clinical criteria for normal and tumor spectrum, i.e. the spectrum with a large Cho and reduced NAA peak is considered a tumor spectrum while a ratio of peak areas of 1/2 is considered normal (46,64).

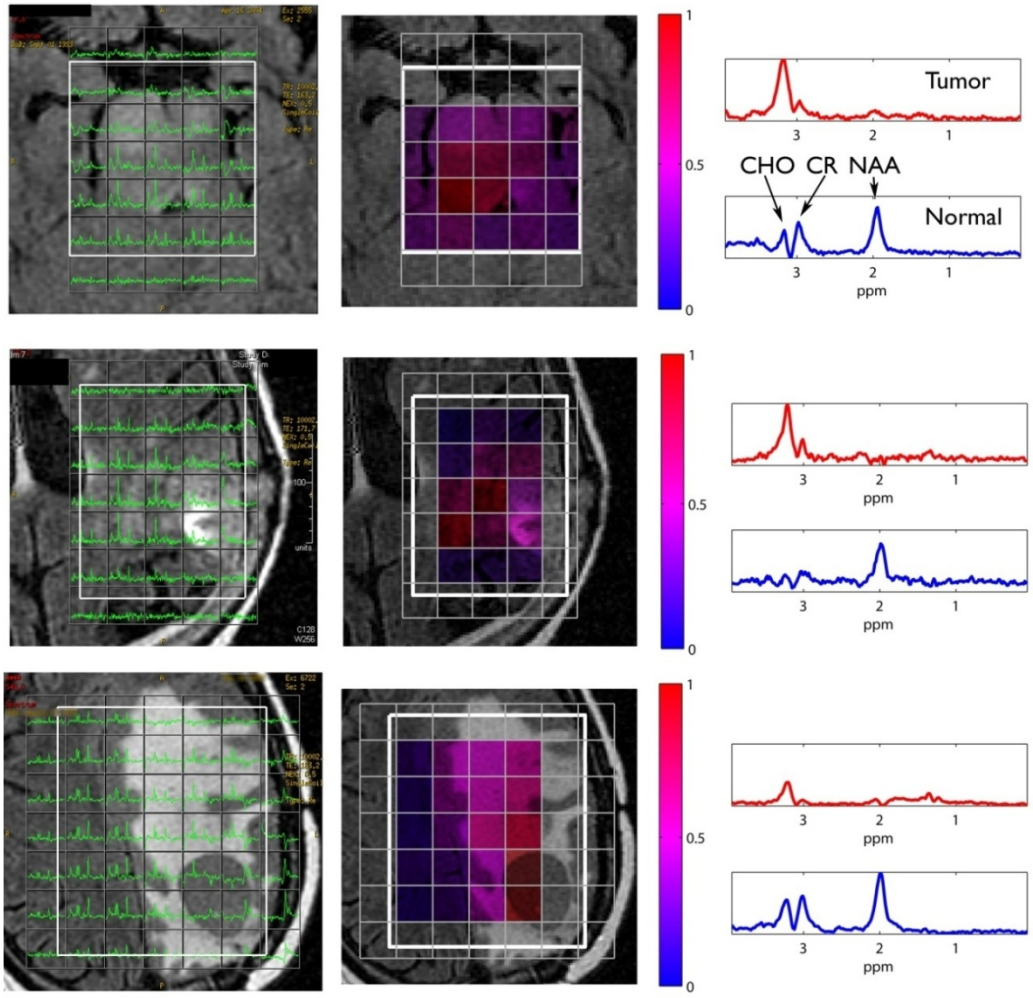

Figure 8: Comparison of conventional processed MRSI spectra with the results of spectrum separation

The left panels show the conventionally processed MRSI multi-voxel spectra overlaid onto a FLAIR image with areas of hyperintensity indicating the abnormal region. The white box represents the region of RF excitation, which is smaller than the field of view of MRSI acquisition. The center panels show the tumor tissue abundance map – column in matrix ***A*** corresponding to the tumor spectrum – merged with the FLAIR image: the redder the area, the more abundant the tumor tissue. For a smooth spatial distribution this colormap has been interpolated between voxels at the same resolution as the FLAIR image. The right panels show the extracted constituent spectra corresponding to the normal tissue and tumor tissue. The constituent tumor spectrum revealed typical pattern of high Cho level and low NAA level.

The present method is similar to Nosologic Images (41) – a previously proposed method for summarizing MRI and MRSI brain-tumor data as a color-coded anatomical image. In that method voxels are classified based on MRSI and MRI data and each tissue class is marked on an MRI image as a separate color (e.g. HGG, LGG or necrosis, normal, etc.). In contrast, the present method only uses spectral information and reports continuous-valued abundance estimates for tumor and normal tissue rather than discrete labels. It thus represents the spatial extent and infiltration of the tumor tissue. It provides an alternative view of the MRSI data to the radiologist, who can then combine this information with the anatomical MRI.

7.2.3 Comparison of Abundance Estimates *A* to Anatomical MRI Data

To validate this abundance-based overlay, we selected the central slice from each of the 20 cases and a neuro-radiologist labeled the voxels in the corresponding slice with "normal", "tumor", "HGG" or "LGG" based on the anatomical MRI information (precontrast sagittal and axial T1-weighted, axial T2-weighted, axial FLAIR, axial diffusion-weighted, and postcontrast T1-weighted images in axial, sagittal, and coronal planes). Those labels were then digitized and used as "truth data" for the receiver operating characteristic (ROC) analysis (96).

To quantitatively evaluate the abundance estimates we calculated the area under the ROC curve (AUC) which indicates the overall performance of a diagnostic test in terms of its accuracy at various diagnostic thresholds. The AUC ranges from 0 to 1 with

0.5 indicating random performance and 1.0 for perfect classification. The results show that the AUC from the 20 cases is 0.90±0.13 for discriminating normal and tumor voxels and 0.91±0.09 for discriminating high grade glioma (HGG) and low grade glioma (LGG) voxels.

Chapter 8 Physiological Relevance of the Decomposition

In this chapter, we are given the physiological and physical evidence to validate the NMF decomposition. The data on clinical ^{1}H MRSI scans of brain tumors in section 8.1 gives strong evidence for the physiological relevance of the extracted spectra $\boldsymbol{S}$. Section 8.2 gives physical evidence to validate the extracted abundance estimates $\boldsymbol{A}$ on a phantom study.

8.1 Validation Physiological Relevance of the Extracted Spectra *S*

8.1.1 Physiological Relevance of the Extracted Spectra *S*

As mentioned in section 2.3, CNI is a conventional quantitative criterion to access spectral abnormality and therefore are widely used to determine the presence of tumor. However the CNI criteria usually fail due to the significant variability of the in vivo spectra which can be introduced by many factors such as tumor heterogeneity, measurement noise, and also partial volume coverage (43,44). Spectrum separation, as proposed here, addresses three sources of variability: 1) Measurement noise is mitigated by combining information across multiple voxels. 2) Partial volume coverage is compensated by explicitly modeling it with an abundance parameter. 3) Tumor

heterogeneity across subjects is accounted for by extracting a tumor spectrum that best matches the specific data set.

To assess the effect on the variability of spectra we contrasted the spectra of high-grade and low-grade gliomas as well as normal brain tissue across subjects. Figure 9 compares the two spectra extracted with the NMF algorithm, which correspond to normal and tumor tissue, and contrast the cases of low-grade and high-grade gliomas. The figure shows the extracted spectra as well as exemplary voxels prior to processing (see voxel selection). In addition, it shows the spectra obtained after averaging over a few voxels to demonstrate the effect that one may expect from (naively) combining multiple voxels. The selecting of representative raw voxel spectra based on FLAIR intensity enhancement and Cho/NAA peak-area ratios follows current conventional practice. Again, only spectra with sufficient SNR were selected (SNR>4dB as discussed in Chapter 6). Spectra from areas with obvious intensity enhancements were selected as tumor spectra. For normal brain we selected only voxels far removed (>2cm) from areas of increased intensity. Because signal quality varies among different datasets, different numbers of voxels were selected for both normal (n=17±11) and tumor (n=15±12) spectra for different datasets. Finally, for each subject, "average" spectra were computed as the mean across these selected voxels for tumor and normal respectively. Evidently the raw spectra are more "noisy" than the average or extracted spectra. The tumor spectra seem to have overall a reduced NAA peak but it seems difficult to find a reliable difference between tumor and normal voxels in the raw spectra. Even for the average spectra the distinction between grades remains difficult.

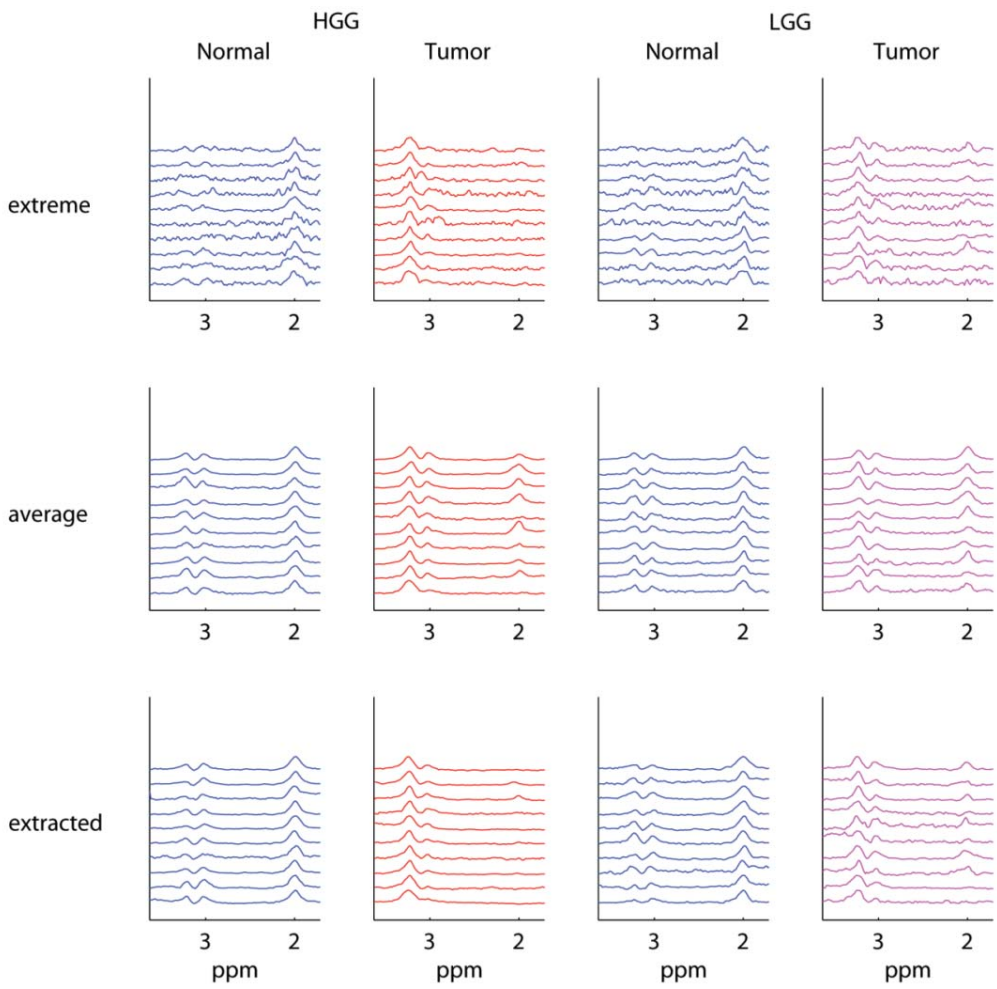

Figure 9: Comparison of raw spectra, averaged spectra, and extracted spectra for 10 patients with LGG and 10 patients with HGG

For each patient two spectra are shown corresponding to normal and tumor tissue respectively. Top graph shows extreme spectra of individual voxel without processing. Here voxel with extreme high and low CNI values are selected as examples for tumor and normal tissue. Center graph show spectra averaged over region with enhanced FLAIR intensity and normal areas. It shows that averaging can reduce the noise. Bottom shows the spectra using the proposed algorithm. These spectra are less noisy and distinguish better between LGG and HGG.

In addition to the "average" spectra mentioned above, within the same selection we also chose one example with an extreme Cho vs. NAA peak area ratio as "extreme" spectrum. This corresponds to current clinical practice which considers the most extreme Cho/NAA ratio as an indicator of tumor malignancy.

To confirm the physiological relevance of the extracted spectra and demonstrate reduction in variability we looked at the Cho and NAA peak areas of the extracted spectra for the 20 available clinical cases with confirmed primary gliomas as shown in Figure 10. Areas were normalized to be independent of an overall (arbitrary) scale. Figure 10a shows the original raw spectra of individually selected voxels for all 20 cases. In order to demonstrate the effect that one may expect from (naively) combining multiple voxels, we compared in Figure 10b the averaged with the ones obtained with the separation algorithm (Fig. 9d). Averaging reduces noise and hence some of the overlap, but is not sufficient to reliably distinguish between normal and tumor tissue. Evidently the overlap of averaged spectra is significantly larger than the extracted spectra. The origin of this reduced variability is two-fold: First, assigning abundance values to each voxel captures and compensates for the variability due to partial volume. Second, computing a single spectrum that is applicable across many voxels reduces estimation variance due to measurement noise. To assess these effects, Figure 10 also shows the results of spectra with extreme CNI (Fig. 10c). Peak areas from the extreme spectra - likely representing pure voxels with 100% volume fraction - show reduced overlap and an improved separation between normal and tumor, and between HGG and LGG. Reduced spectral variability manifests itself in a better differentiation of the three tissue types after separation (HGG, LGG, and Normal).

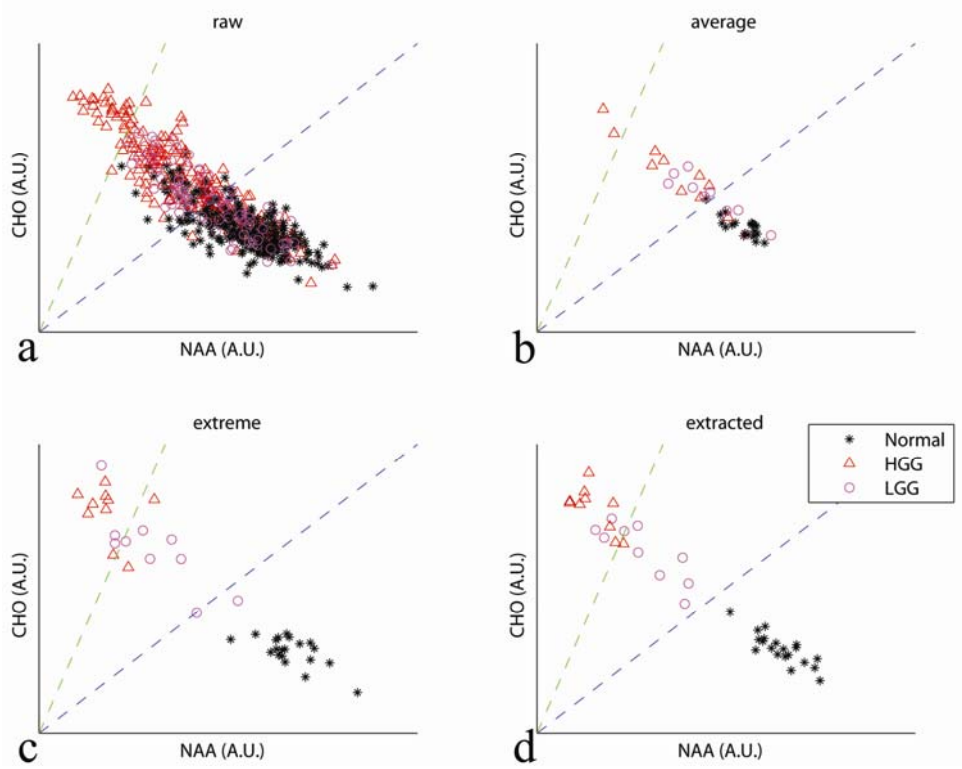

Figure 10: Validation of extracted spectra *S* with pathologically proven tumor grades

10a, Cho versus NAA peak areas (in arbitrary units) for voxel spectra from all 20 patients, taken from the individual MRSI voxels located in the regions of FLAIR hyperintensity and surrounding normal appearing areas before the NMF analysis. Points indicate maximum peak areas for spectra over the following frequency ranges: Cho 3.34–3.14 ppm and NAA 2.22–1.82 ppm. The colored symbols are for spectra from tumor voxel in the area of hyperactivity. LGG are shown as magenta circles, while HGG are shown as red triangles. The NAA and Cho peaks from voxels of normal brain tissue are shown as black asterisks. There is significant overlap in voxel spectral pattern between the HGG, LGG, and the normal appearing regions. Dashed blue and green lines show the Cho/NAA ratio of 1 and 3 respectively. **10b,** Averaged Cho and NAA levels across voxels for each individual patient. Averaging across voxel reduces noise but significant overlap remains. **10c,** Cho and NAA levels of the extreme spectra (see voxel selection) from all 20 patients. Compared with b, overlap is reduced and better separation is achieved. **10d,** The same type of plot of the constituent tumor and normal tissue spectra from all 20 patients following the NMF analysis. As with the average spectra each of the 20 cases contributes two points corresponding to the extracted spectrum for normal and tumor tissue. The Cho-NAA patterns of the normal spectra were well separated from those of the tumor spectra. The separation is sufficient for distinguishing Tumor vs Normal and HGG vs LGG (see table) and matches very well with the clinical criteria based on Cho/NAA ratio (dashed blue and green lines).

8.1.2 Reduced Variability on Clinical Scans

To quantify the reduction in variability we measured the coefficient of variation (CV) of CNI. In probability theory and statistics, the CV is a normalized measure of dispersion of data points in a data series around the mean. It represents the ratio of the standard deviation to the mean:

$$\text{Coefficient of Variation} = \frac{\text{Standard Deviation}}{\text{Mean}}$$

The statistic was computed for Cho and NAA based on maximum peak areas of the extracted spectra. To normalize for the arbitrary scale of the spectra we used the Cr peak area. Specifically, peak area of Cr, Cho and NAA were scaled to sum to one. Hence, NAA and Cho were given in arbitrary units (a.u.) that are insensitive to scale. Note that this operation preserves linear separability of the data (separating lines in Figure 10 remain lines for any such scaling transformation).

The result shows that the CV of CNI is reduced for LGG but not HGG cases. Since the CV for different tissue classes (normal, HGG and LGG) are not all normally distributed (Doornik-Hansen Omnibus multivariate normality test), parametric test could not be applied to evaluate the statistical significance of the changes in CV. Given the nature of the sample in the current study - small and with no prior knowledge on the distribution of the CNI CV - it would be most appropriate to perform this study using a non-parametric resampling scheme: bootstrapping.

Bootstrapping is a non-parametric method for calculating a sampling distribution for a statistic (97). It calculates the statistic with *N* different subsamples. The idea behind bootstrapping is that if the sample is a good approximation of the population, the sampling distribution of interest may be *estimated* by generating a large number of new samples from the original sample. Put another way, bootstrapping treats the sample as if it is the population. There are two main advantages of bootstrapping: First, bootstrapping can be used to estimate the sampling distribution of any well-defined function of sample data. Therefore it is especially useful in situations for which no analytic formula for the sampling distribution is available and/or it is intractable (i.e., no look-up table for critical values is possible). Second, Bootstrapping makes no assumption about the population (no normality and equal variance assumptions, not even the central limit theorem), other than the assumption of random sampling. So it is useful when required assumptions of a test are clearly violated. For example, the t-test with two independent sample means requires the equal variance assumption. If this assumption is violated and sample sizes are not large, the test cannot be used and no other alternative exists.

We performed bootstrapping (98) by resampling the CV of CNI with replacement. The resampling was done by drawing 1000 "resamples" of size N=20 from the original 20 samples randomly with replacements. The result showed no significant changes probably due to small sample size.

To overcome the limitation of a small sample size, we simulated LGG and HGG cases with mean Cho/NAA ratios of 2 and 2.3 respectively (42,99,100). Variability across subjects and voxels was modeled by adding variability to these mean Cho/NAA

ratios. Variance was adjusted to match the classification performance between LGG and HGG on the extreme spectra. This simulated data was used to estimate classification performance and coefficient of variation on a larger sample.

We simulated data for a larger sample size (60 cases of HGG and LGG respectively) and found indeed significant reduction in CV (change in CV of 3.39±0.09 for HGG, p=0.002, and 4.07±0.09 for LGG, p=0.0003, N=120).

To judge whether the changes in CNI CV is statistically significant we focus now on the ability of the data to deliver a diagnosis on an individual subject basis. In general, the proposed method delivers multiple spectra and peak areas and diagnosis may require a multivariate discrimination technique (41). On the present data, however, it was sufficient to consider the ratio between Cho and NAA peak areas. This specific linear discrimination criterion is captured by the CNI. The conventional figure of merit for classification which captures sensitivity at various levels of specificity is the area under the ROC curve (AUC) (96). ROC curves are shown in Figure 11. Mean and standard deviation for the AUC were calculated with the bootstrapping method as mentioned above (resampling from 20 cases with replacement) (98). The diagnostic specificity to distinguish LGG and HGG for extreme and extracted cases is substantially increased from 0.83 to 0.89. To evaluate the statistical significance of this improvement, we compared the two AUC by a nonparametric approach proposed by DeLong et al. (101). The result showed no statistical significance of the diagnostic specificity to distinguish LGG and HGG probably because of the small sample size (10 LGG and 10 HGG cases).

To determine the sample size needed for sufficient statistical power we performed the power analysis and sample size estimation. In statistical analysis, the p-value is determined by three factors: observed effect, sample size, and/or criterion required for significance (alpha). The larger the observed effect, the larger the sample size, and/or the more liberal the criterion, the more likely it is that the test will yield a significant p-value. These three factors and the statistic power form a closed system, in which once any three are established, the fourth is completely determined. Statistical power analysis and sample size estimation are the usually used methods to determine how likely we would achieve statistical significance with a particular sample size assuming true difference between groups.

In the current study power analysis was performed as follows: two normally distributed data were synthesized with same standard deviation but different mean. Mean was adjusted to match the classification performance between LGG and HGG on the extreme spectra (AUC=0.82). We then performed a Monte Carlo simulation for different sample sizes. For a specific sample size N (ranging from 5 to 60) we drew N samples from each normal distribution and calculated the AUC value 1000 time. This gave us an empirical distribution of the AUC as a function of the sample size. We approximated the best N such that the empirical distribution yields a p-value of 0.05 for AUC value of 0.89 (AUC of the extracted case).

The result indicated that a significant difference for the 6 point improvement in AUC would require at least 60 samples (101), i.e., a sample roughly 3 times the size we currently have. We therefore simulated a larger data set with parameters and performance

that match the clinical data and found a significant improvement in AUC (p=0.009) with a sample size of 30 LGG and 30 HGG cases.

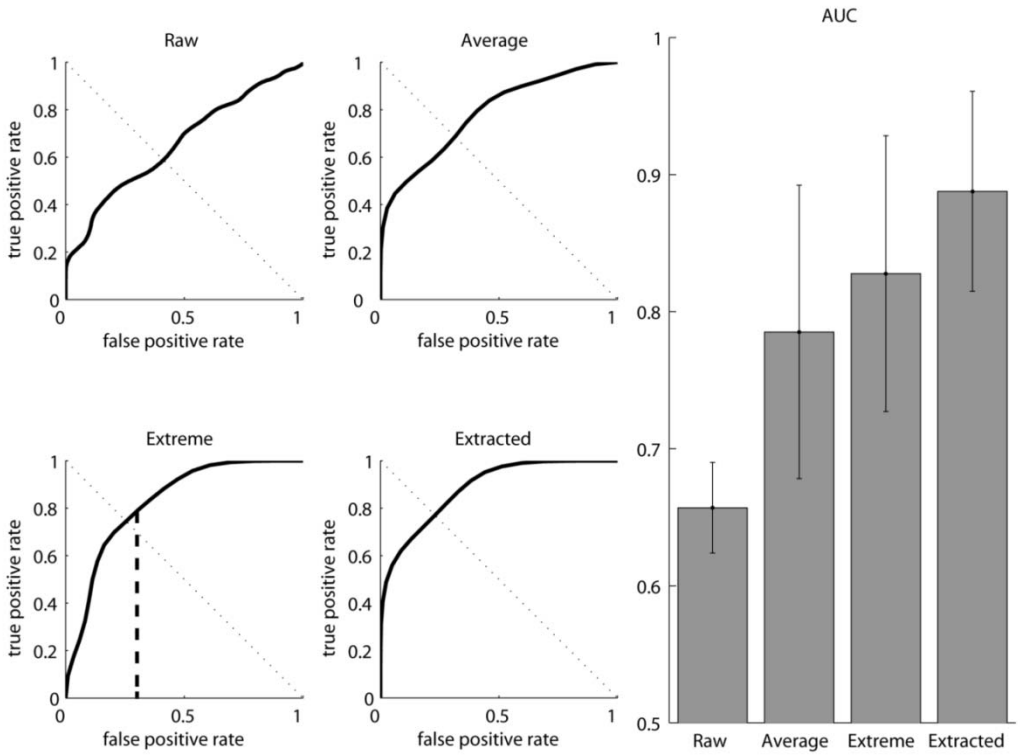

Figure 11: Classification of performance between HGG and LGG using CNI criterion

Four panels on the left show ROC curves estimated using a bootstrapping procedure. CNI diagnostic criterion (CNI=3) is indicated as straight dashed line for the extreme spectra following clinical convention. Mean AUC for all four conditions is summarized on the right. Error bars indicate the standard deviation of the bootstrapping procedure. Diagnostic performance on this data is improved substantially by using extracted spectra (AUC=0.89) as compared to current clinical practice of using extreme spectra (AUC=0.83).

Table 1: Discriminability for raw, average, extreme and extracted spectra

Comparison	Metric	Raw voxel spectra	Average spectra across voxels	Extreme voxel spectra	Extracted constituent spectra
Normal vs. Tumor	Discrimination (AUC)	80%	90%	100%	100%
LGG vs. HGG		67%	78%	83%	89%

The first conclusion from Figure 10, 11 and Table 1 is that the extracted spectra are physiologically meaningful and can be given a clinically significant interpretation. Secondly, the reduced variability is reflected in an improved diagnosis.

8.2 Validation of Abundance Estimates *A* as Volume Fraction on a Phantom

Having estimates of tumor abundance for each voxel suggests that it may be possible to detect the presence of a malignant tumor even at low volume fractions where the current method based on CNI fails: Small volume fraction within a voxel reduces CNI for an otherwise highly malignant tumor. Therefore, accurate abundance estimates $\boldsymbol{A}$ could be used for tumor detection in this regime of low volume fraction. This should result in increased detection *sensitivity* in addition to the improvement in *specificity*

resulting from reduced spectral variability of estimates ***S***. This is particularly important given that diagnosis and treatment are typically based on the most malignant tumor, which may at first only be present in small volume fractions.

To empirically validate the accuracy of the abundance estimates we built a cylindrical phantom (Plexiglas) with two semi-cylindrical chambers, which were filled with solutions containing Cr and NAA at concentrations corresponding to normal brain tissue (NAA: 10.43mM; Cr: 7.49mM) and tumor tissue (NAA: 5.21 (=10.43/2) mM; Cr: 14.98 (=7.49x2) mM) respectively. Note that with this choice we expected a factor 4 for the difference in the Cr/NAA ratio between the spectra of the two chambers. Cho has not been included due to poor stability in the solution. FLAIR and MRSI data were obtained ensuring partial coverage of voxels across the boundary of the chambers as shown in Figure 12. Data were recorded using the same acquisition parameters as in the clinical scans and were processed in the same fashion, resulting in the spectra with an SNR of 11.5±0.7dB (n = 5). All voxels inside the excitation box were selected to validate the accuracy of the abundance estimates.

As shown in Figure 12, NMF algorithm recovered spectral profiles with peak areas that correspond to the concentration in each solution. The "normal" spectrum shows a displacement of the Creatine (Cr) peak, which would have been expected at 3ppm. This shift is evident also in the original spectra of the lower chamber (see Figure 12). Since the algorithm is adaptive it has no difficulty in extracting this unexpected spectral profile. This demonstrates that the method correctly decomposes the observed data into

constituent spectra corresponding to the different solutions with their specific metabolite concentrations.

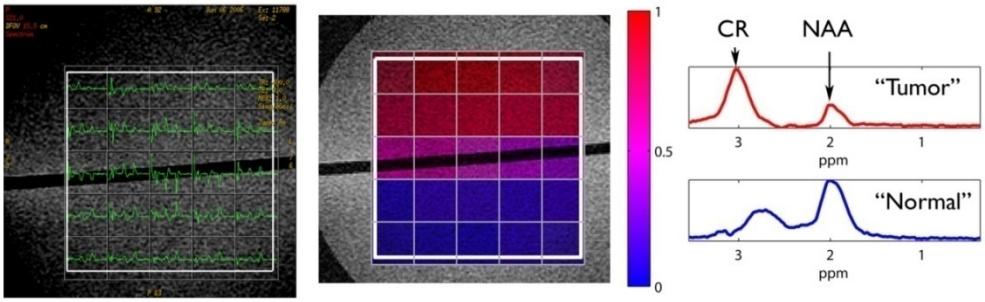

Figure 12: Results of spectrum separation on phantom study

Display same as in Figure 8. The two chambers were filled with Cr and NAA in a water solution at concentrations corresponding to tumor tissue (upper chamber) and normal brain tissue (lower chamber). The overlay in the center panel shows a good match between the estimated abundance ***A*** and the actual volume fraction (see also Figure 13). This indicates the method correctly decomposes the observed data into the constituent spectra corresponding to the different solutions with their specific metabolite concentrations. The Cr/NAA peak ratios for the two spectra differ by a factor of 4 as expected.

To quantify the accuracy of the abundance estimates, we show in Figure 13a the relationship between the actual volume-fraction covered by each voxel (real ***A***) as determined from the geometry of the overlay shown in Figure 12 and the abundance estimates from the NMF algorithm (estimated ***A***). A sigmoid function was used to model the relationship between real abundance and the estimated abundance:

$f(x) = \left(1 + \exp\left(-c - b\,x\right)\right)^{-1}$, where x represents the real abundance and f represents the abundance estimates. 95% confidence intervals were then calculated to quantify the accuracy of the abundance estimates using standard methods (102-104).

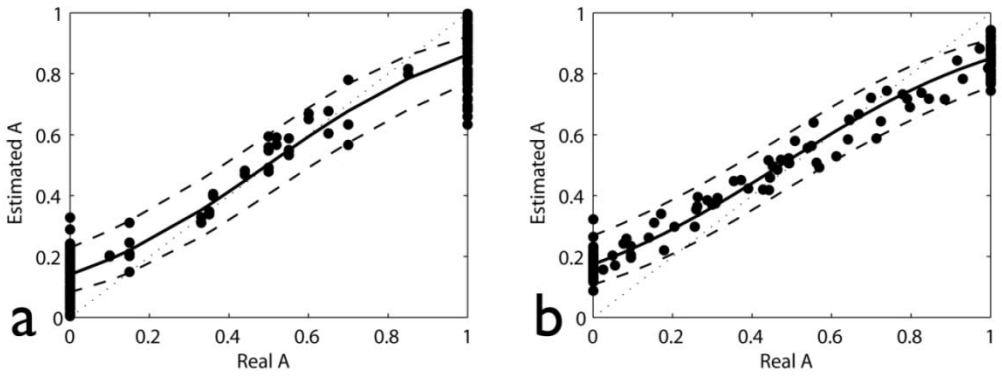

Figure 13: Validation of the estimated abundance *A* on phantom study and simulated data

13a, Horizontal axis gives the actual volume-fraction of the "tumor like" spectrum (real ***A***), which is calculated based on the geometry of the phantom in Figure 11. Pure voxels in the upper chamber corresponding to "tumor like" metabolite concentrations are given abundance values = 1, while pure voxels in the lower chamber have abundance values = 0. Voxels covering the chamber boundary have intermediate values based on the fraction of volume covered. Vertical axis gives the estimated abundance of "tumor like" spectrum as computed by the NMF algorithm (estimated ***A***). Dotted line indicates 100% accuracy estimation. Solid and dashed lines are the sigmoid fitting curve and the 95% confidence intervals. **13b**, The same plot as in (a) on simulated data with randomly chosen volume-fractions and noise. Simulation was repeated 100 times to estimate the mean and confident intervals. Sample points shown are a subset of these repetitions. Horizontal axis gives the predefined volume-fractions. Vertical axis gives the abundance estimates computed by the NMF algorithm.

The result shows that the values are better estimated for intermediate-ranged abundances than for high and low abundance estimates where one can see an upward and downward bias, which will be discussed in the following section. The 95% confidence interval is significant throughout. It may result from the noise of the measurements. This noise is evident already in the pure voxel spectra as shown in Figure 14.

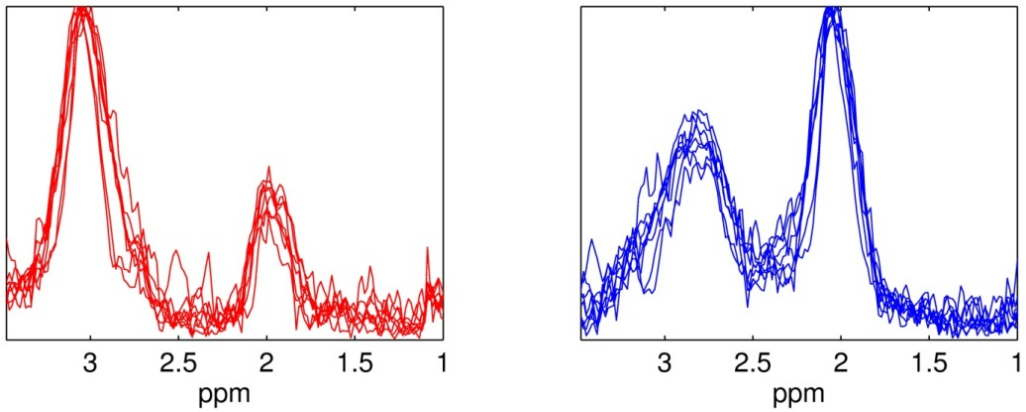

Figure 14: Pure voxel spectra from the phantom study

Spectra on the left are the sample "tumor like" spectra from one of the semi-cylindrical chambers, which were filled with solutions containing Cr and NAA at concentrations corresponding to tumor tissue (NAA: 5.21 (=10.43/2) mM; Cr: 14.98 (=7.49×2) mM). Spectra on the right are the sample "normal like" spectra from another semi-cylindrical chamber, which were filled with solutions containing Cr and NAA at concentrations corresponding to normal brain tissue (NAA: 10.43mM; Cr: 7.49mM).

Finally note that, confronted with noise (and distortions) the decomposition returns the correct spectra $\boldsymbol{S}$ (as reflected by correct peak ratios in Figure 12) but makes a biased estimate on abundances $\boldsymbol{A}$. The linear decomposition permits $\boldsymbol{A}$ to be adjusted to every voxel, however, it is forced to use the same $\boldsymbol{S}$ across all voxels. Hence, variability across voxels due to noise and distortions can only be captured by $\boldsymbol{A}$, leaving the estimate for $\boldsymbol{S}$ largely unaffected.

8.3 Abundance Estimation Bias

Accurate abundance estimates are particularly useful in delineating tumor extent for the planning of radiation and surgical treatment. In the current study the phantom is

used to explore the estimation accuracy of abundances and results show an upward and downwards estimation bias. The possible reasons for the observed bias are discussed as follows:

8.3.1 Non-Linearity Distortions

One possible reason is the violation of the linear assumption required by the NMF algorithm of using absolute spectra. To test this hypothesis, we performed a simulation study to compare the relationship between the actual volume-fractions and the abundance estimates. Two 8x8 slices of simulated MRSI data containing H_2O, NAA and Cho were generated as described above with one slice corresponding to a Cho/NAA ratio of 2, and a second slice to a ratio of 1/2. The third slice was generated by linearly mixing the first two slices with various volume-fractions (selected at random) for each voxel. To assess the estimation variance this simulation was repeated 100 times with different randomly selected volume-fractions and Gaussian noise at 11.5dB (R^2=0.98). The simulated data was preprocessed and submitted to the NMF algorithm. The abundance estimation matrix $\boldsymbol{A}$ was compared with the predefined volume-fractions to evaluate the accuracy of the abundance estimates.

Figure 13b shows the relationship between the actual volume-fractions and the abundance estimates on simulated data with an SNR comparable to the phantom data. The result shows a similar pattern to the one in Figure 13a. The same simulation study performed at 4dB (R^2=0.85) which is the minimum required for the clinical data, shows a

comparable bias with an increase in the confidence intervals. This indicates that the poor abundance estimates in high and low volume fractions are due to a systematic bias. A modified NMF separation algorithm, such as semi-NMF (105), may be able to fix the bias since it does not require the non-negativity constraint. Semi-NMF will be discussed in detail in Chapter 10

8.3.2 Magnetization Transfer (MT) Effects

In addition to the violation of linearity that could introduce estimation bias, other factors may also contribute to the biased estimates. As we discussed in the previous section, the spectra from pure voxels of the phantom experiment are quite noisy as shown in Figure 12 and Figure 14. Moreover, there is a displacement of the Creatine (Cr) peak in the "normal" spectrum. This shift is also evident in the original spectra of the lower chamber (see Figure 12 and Figure 14). The algorithm is adaptive and it has no difficulty in extracting this unexpected spectral profile. However, we wonder what might be the reason for the shift as it may affect the estimation process since the spectrum is not homogeneous across voxels.

One possible reason for the unexpected shift is that there might be considerable field distortions during the data acquisition. Remember that the theoretical analysis suggests the fields distortions ΔB will lead to frequency shift and stretch ($\frac{v-\Delta B/B_0}{1-\Delta B/B_0}$) for the same factor $\Delta B/B_0$. In the current routine of frequency alignment we only correct the frequency shifts but ignore the stretching of the spectra. It is reasonable for the clinical

data since the overall shift and stretch is small (~0.03ppm). But for the phantom (Figure 12 and Figure 14), we noticed that the frequency shift for the phantom is quite big (~0.3ppm). In the presence of this significant frequency shift, to perform the frequency alignment by simply shifting the spectra might not be sufficient and consequently leads to the biased abundance estimates. According to the theoretical analysis, it may be helpful to include the spectral stretching to the routine of frequency alignment for the phantom data. But the spectra from Figure 12 and Figure 14 also show that the shift is only present in the "normal" part of the phantom. The "tumor" part shows correct frequency component of Cr and NAA. There might be field fluctuations during the data acquisition, but it is not likely that the filed inhomogeneity only exists in one side of the phantom while the other side is uniform.

Since the abnormality of the spectra only happens in the "normal" part of the phantom, another possible reason for the shift might be a chemical exchange or reaction in the "normal" part of the phantom for this particular NAA vs Cr concentration composition. Because Choline is sensitive to light and easily degraded, in the phantom study Cr (a more stable substance) was used as a substitute to mimic the "real situation" instead. There is a phenomenon called magnetic transfer (MT) which often occurs between water and Creatine in NMR spectroscopy experiments, especially for spectra acquired in solution.

Magnetization transfer (MT) effects occur if one spin pool exchanges magnetization with one or several other spin pools. It was accidentally discovered by Wolff and Balaban in 1989 (106). In MRI of molecular solutions, there are two types of

water molecules: free (bulk) and bound (hydration). Conventional MRI is based primarily on free (bulk) water protons. The T^2 relaxation times for bulk water protons are greater than 10ms and detectable, while T^2 relaxation times of protons associated with macromolecules are less than 1ms and non-detectable in MRI. MT may happen between bulk water protons and macromolecular bound proton when an off resonance radio frequency pulse is applied to the macromolecular protons. The saturation of these protons is then transferred to the bulk water protons. The result is a decrease in signal (the net magnetization of visible protons is reduced), depending on the magnitude of MT between tissue macromolecules and bulk water.

There are reports indicating that Cr is one of the metabolites associated with the strongest MT effects (107-111). ^{1}H NMR spectra from animal or human brain or on skeletal muscle indicate that MT affects the signal intensity of Cr. It is also emphasized that MT effects caused by water suppression techniques may lead to systematic errors in the quantification of *in vivo* ^{1}H NMR spectra since the water suppression techniques will affect the inversion recovery of water. De Graaf *et al.* discussed this problem where the influence of different water suppression techniques on proton spectra of the rat brain was compared. The result suggested that water suppression by the CHESS sequence performs the best. There, no significant changes of metabolite signals were found (107). It is important to note that the negligible effect of CHESS observed by de Graaf *et al.* is based on the short delay between the water suppression pulses and the signal excitation pulses of the MRS sequence as well as on a rather slow exchange of magnetization between different spin pools. Different to the results of de Graaf *et al.*, Kreis *et al.* reported that CHESS caused signal changes of Cr in measurements on human muscles (109). In proton

spectra measured on the Langendorff perfused rat heart, Schneider *et al.* observed a signal decrease for Cr if CHESS (with a rather long delay between water suppression and excitation of the metabolites) was used (111). Thus, one should emphasize that whether or not water suppression techniques cause changes in metabolite signals depends on the specific sequence parameters used, in particular the time provided for spin exchange.

In this study, CHESS sequence was used in both clinical data and phantom data for water suppression. Some degree of MT effect of Cr may not significantly affect the result of our spectral analysis for the clinical data since the two most important metabolites we are interested in, Cho and NAA, show negligible MT attenuation (107,108,110). But for the phantom study, the use of Cr might introduce considerable MT effects. As a result, the decreasing of Cr signal would lead to a systematic underestimation of metabolite concentrations in each voxel. As we discussed before, the variability across voxels due to noise and distortions can only be captured by $\boldsymbol{A}$, leaving the estimate for $\boldsymbol{S}$ largely unaffected. If the Cr signal in each spectrum of the phantom is decreased by certain amount, this modification of the raw data will eventual cause the abundance estimation bias.

From the above discussion of the estimation bias observed from the phantom study, besides the possible reason of the nonlinear distortions, the MT effects between water and Cr might be another reason for the algorithm extracting biased abundance estimates. The details of the MT effects on the phantoms data requires further experiments. More reliable chemicals and proper designed acquisition sequence will be needed to further quantify the accuracy of the abundance estimates.

Chapter 9 Spectrum Separation Characterizing Tissue Heterogeneity

The proposed method extracts homogeneous spectra for normal and tumor tissues. But this assumption might not be true, especially for tumor spectra which usually do not always show a unique and stable spectral pattern. The pattern of tumor spectra may differ for tumors of different grades and types, even within the same tumor due to the heterogeneity of tumor tissue itself. This chapter will discuss about how the present study deals with this issue.

As mentioned before, the only parameter of NMF that needs to be determined is the dimensionality of the matrices $\boldsymbol{A}$ and $\boldsymbol{S}$, namely the number of constituent spectra to recover. In the current study PCA suggested to use two basic sources, i.e. normal and tumor (Figure 7). But if sufficient diversity in the spectra is apparent, one can modify the number of the basic sources and decompose the data into multiple constituent spectra to capture this heterogeneity.

Figure 15 shows an example of the data from a patient with HGG and a necrotic region. When decomposing the data into 3 spectra, the abnormal spectra are further decomposed into a high grade tumor spectrum (Cho/NAA=5) and a high lipid spectrum. It is clear that the proposed method successfully give a distribution of normal, necrotic, and tumor tissue. Therefore if sufficient diversity in the spectra is apparent, e.g. lactate

and lipid peaks are present, then one can extract more than one tumor type provided the corresponding frequency range is included.

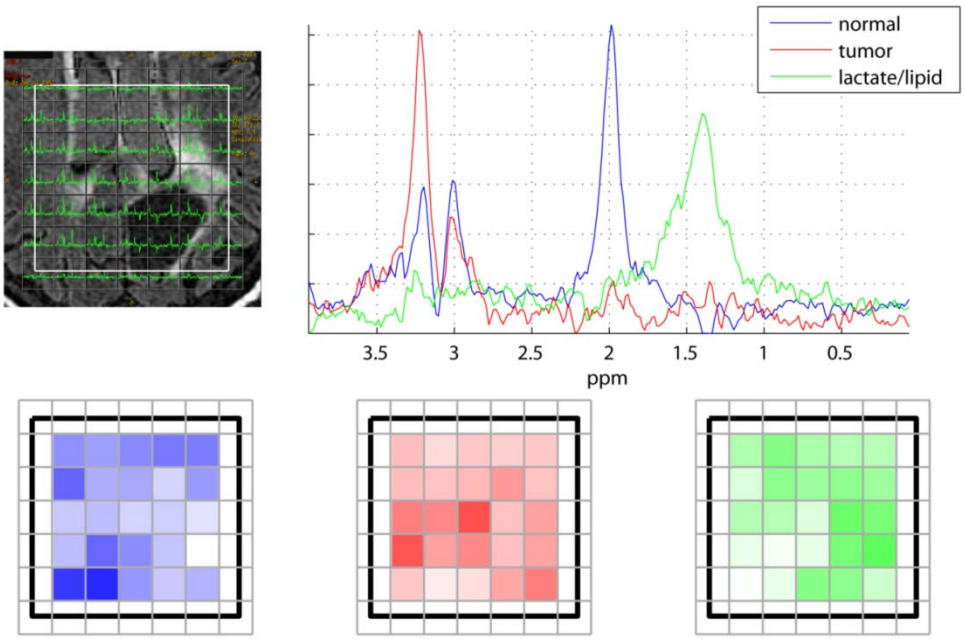

Figure 15: Results of spectrum separation on data with clear lipid peaks

Figure on the top left corner shows MRSI multi-voxel spectra overlaid onto a FLAIR image with clearly present of lipid/lactate (~1.5ppm). Figure on the top right shows the three constituent spectra. In this case of clear lipid peak, the third spectrum represents the lipid/lactate distribution. The three figures in the bottom show the corresponding abundance estimates.

Result from the above example shows that our proposed method has the potential in differentiating necrotic tissues from residual tumor tissues by incorporating this additional lipid/lactate information into the current classification methodology. Since the lactate and lipid peaks are known to be predominantly present in HGG, usually in necrotic areas where high Cho may not be present, adding this information into the analysis may improve classification accuracy. Therefore, if sufficient diversity in the

spectra is apparent, one can modify the number of the underlying sources, i.e. the dimensionality of the matrices $\boldsymbol{A}$ and $\boldsymbol{S}$, and decompose the data into multiple constituent spectra to capture the tissue heterogeneity.

In addition, the "truth-labels" provided by the neuro-radiologist indicating normal, necrotic, solid, and edematous regions based on MRI/MRSI may serve as further selection criteria prior to the application of the separation method thus addressing a major concern on tissue/spectral hetereogeneity.

Chapter 10 Semi-Nonnegative Matrix Factorization

Abundance estimates from the decomposition can be used to distinguish currently ambiguous scenarios: partial coverage of a high-grade tumor versus complete coverage of a low-grade tumor. Essentially the goal is to increase sensitivity in detecting aggressive tumors at the tumor margins. This is of particular importance in the planning of radiation therapy which should ensure complete coverage of proliferate tissue while sparing healthy tissue as much as possible. Data in section 8.2 validates the abundance estimates on a phantom study showing a good match between the actual volume fraction (from the geometry of the phantom) and the estimates from the NMF algorithm. It also establishes confidence intervals for these estimates.

Furthermore, we found that the abundance values in the intermediate range are better estimated than that of the low and high volume fractions. There is an upward and downward estimation bias at the extremes. A possible explanation is the violation of the linearity assumption. In theory MRSI data acquisition and spectral data analysis guarantees linearity. However, to avoid problems associated phase distortions resulting from field inhomogeneities we opted to use in this study the magnitude spectrum rather than the conventional absorption spectrum. While this guarantees positive spectra and resolves potential inconsistency across voxels, it does introduce a non-linear distortion as a result of the absolute value operation.

Other than introducing a threshold constraint on ***S*** (cNMF) as discussed previously, another solution to deal with the possible negative values in the observations ***X*** is to apply a factorization which does not require the nonnegative data matrix. The motivation is to apply a general factorization in which ***A*** is restricted to be nonnegative and ***S*** is unconstrained.

10.1 Semi-Nonnegative Matrix Factorization (semi-NMF)

Since the introduction of the Nonnegative Matrix Factorization (NMF) algorithm by Lee and Seung (71), the NMF approach has been cast into alternate formulations by various researchers. For example, Chris Ding has proposed a new variant of NMF with enhanced interpretability called semi-NMF (105). By modifying the updating rules of Equation (3.3), this variation allows the data matrix to have mixed signs, which makes the algorithms better suited for MRSI data as compared to the current NMF algorithm.

In the semi-NMF algorithm Equation (1.1) is revised in the following format:

$$X_{\pm} = A_{+} S_{\pm} + N \tag{10.1}$$

In this formula, the observation ***X*** is allowed to have mixed signs. ***S*** typically has entries with both positive and negative signs (unconstrained) while ***A*** remains nonnegative. The modified multiplicative update rules for ***A*** and ***S*** are:

$$S_{\lambda,m} \leftarrow \left(S_{\lambda,m}\left(A^{T} A\right)^{-1}_{m,m}\right)^{-1}$$

$$A_{i,m} \leftarrow A_{i,m} \sqrt{\frac{\left(X^T S\right)^+_{i,m} + \left[A\left(S^T S\right)^-\right]_{i,m}}{\left(X^T S\right)^-_{i,m} + \left[A\left(S^T S\right)^+\right]_{i,m}}}$$

where + and – denote the positive and negative parts of a matrix G are separated as:

$$G^+_{i,m} = \frac{\left(\left|G_{i,m}\right| + G_{i,m}\right)}{2}, \qquad G^-_{i,m} = \frac{\left(\left|G_{i,m}\right| - G_{i,m}\right)}{2}$$

The initialization step for semi-NMF is different from cNMF. In the cNMF, the initialization starts from random selection of $\boldsymbol{A}$ followed by initializing $\boldsymbol{S}$ via the least squares optimization. In the semi-NMF, a K-means clustering is used for initializing $\boldsymbol{A}$. This gives cluster indicators $\boldsymbol{A}$: $\boldsymbol{A_{i,m}} = 1$ if X_i belongs to cluster m. Otherwise, $\boldsymbol{A_{i,m}} = 0$. A small constant (we use the value 0.05 in practice) is adjusted to all elements of $\boldsymbol{A}$ with proper normalization (sum up to 1 between clusters). The convergence proof for semi-NMF is given in (105).

10.2 Application of Semi-NMF Algorithm on a Phantom

To investigate the applicability of the semi-NMF algorithm on MRSI data and to validate the accuracy of the abundance estimates obtained from semi-NMF we show in Figure 16 the result from the phantom study. The spectral profiles and the abundance estimates recovered by the semi-NMF algorithm show comparable results as with the factorization by current NMF algorithm (Figure 12). Recovered spectral profiles with

peak areas corresponding to the concentration in each solution demonstrate that the method correctly decomposes the observed data into constituent spectra that correspond to the different solutions with their specific metabolite concentrations.

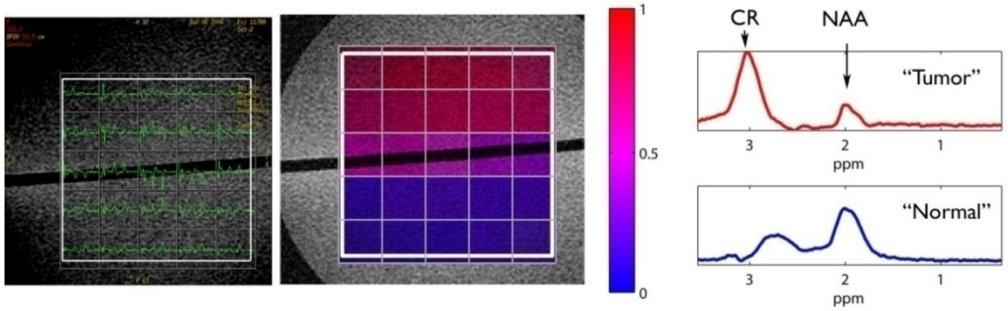

Figure 16: Results of spectrum separation on phantom study by semi-NMF

The two chambers were filled with Cr and NAA in a water solution at concentrations corresponding to tumor tissue (upper chamber) and normal brain tissue (lower chamber). The overlay in the center panel shows a good match between the estimated abundance ***A*** and the actual volume fraction (see also Figure 17). This indicates the method correctly decomposes the observed data into the constituent spectra corresponding to the different solutions with their specific metabolite concentrations. The Cr/NAA peak ratios for the two spectra differ by a factor of 4 as expected.

To quantify the accuracy of the abundance estimates, we show in Figure 17a the relationship between the actual volume-fraction covered by each voxel (real ***A***) as determined from the geometry of the overlay shown in Figure 16 and the abundance estimates from the semi-NMF algorithm (estimated ***A***). The result shows a similar pattern compared with that from the current NMF algorithm (Figure 17b).

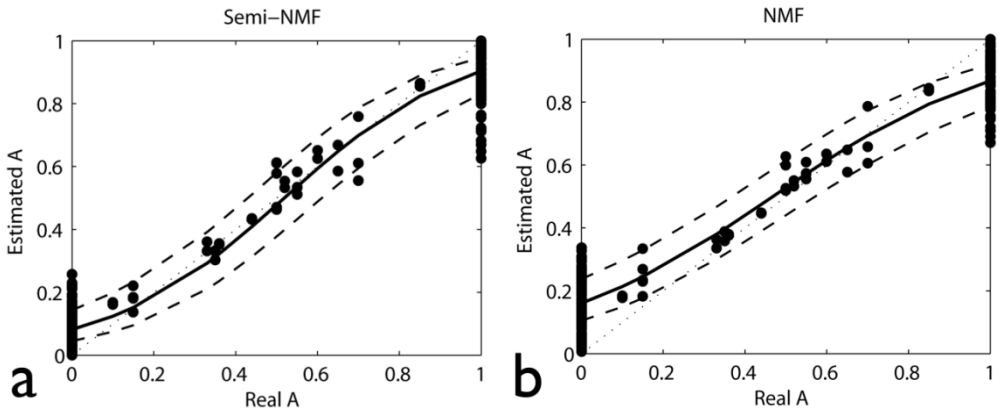

Figure 17: Validation of the estimated abundance *A* on phantom study by the semi-NMF algorithm and by current NMF algorithm

17a:Horizontal axis gives the actual volume-fraction of the "tumor like" spectrum (real ***A***), which is calculated based on the geometry of the phantom. Pure voxels in the upper chamber corresponding to "tumor like" metabolite concentrations are given abundance values = 1, while pure voxels in the lower chamber have abundance values = 0. Voxels covering the chamber boundary have intermediate values based on the fraction of volume covered. Vertical axis gives the estimated abundance of "tumor like" spectrum as computed by the semi-NMF algorithm (estimated ***A***). Dotted line indicates 100% accuracy estimation. Solid and dashed lines are the sigmoid fitting curve and the 95% confidence intervals.**17b**: Relationship between the actual volume-fraction and the abundance estimates from the NMF algorithm (the same plot as Figure 13a).

The above results show that semi-NMF has similar performance compared with the current NMF algorithm with perhaps a reduced bias at the low and high abundances. Since it allows observations to have negative values, as a result the real spectra can be used to avoid the linearity violation. It therefore shows some potential in further improving the estimation bias.

The results indicate that this generalized factorization algorithm is more suitable for MRSI spectral analysis and semi-NMF can be a valuable tool if we can improve data quality with better field stability and phase correction approaches.

Chapter 11 Summary and Future Work

11.1 Summary and Achievements

The advent of clinical MR imaging in the 1980s heralded a new era in the ability to image the brain *in vivo*. MRI allows the detailed depiction of brain anatomy and pathology with unprecedented spatial resolution and soft-tissue contrast. MR spectroscopy imaging is one of the important physiological MR techniques providing metabolite levels within different tissues and important surrogate markers of disease pathophysiology or therapeutic response.

The application of MR spectroscopy to *in vivo* studies provides unique information on tissue chemistry, and these measurements are widely used for diagnostic clinical studies and basic biomedical research. Over the last decade there has been a tremendous increase in both, the variety and quantity of MR spectroscopy data acquired from *in vivo* studies. This has led to the development of new methods of analysis, beyond the traditional peak integration and single spectrum fitting procedures to extract a maximum of information contained in the data.

In this study, we developed data conditioning routines for brain tumor MRSI data in both time and frequency domain. With regard to the problematic phase encoding artifacts, we performed a theoretical study investigating how the most common phase

distortions propagate into NMR data and revealed the logic behind each preprocess procedure for the frequency domain spectral analysis.

Furthermore, we developed a novel quantification tool for magnetic resonance spectroscopic imaging (MRSI) and evaluated its clinical relevance on routine scans of brain tumor patients. The statistical approach, which is based on a blind source separation algorithm, is called nonnegative matrix factorization (NMF). The algorithm simultaneously decomposes the recorded MRSI data into two non-negative matrices representing (a) the underlying tissue-specific spectral patterns and (b) the spatial distribution of the corresponding metabolite concentrations. By representing each spectrum as a linear combination of constituent spectra one obtains a set of spectra that are the same across many voxels, i.e the variability due to volume effect is minimized. In addition, one obtains spectral images, which quantify the relative abundance of tissue types contributing to the observed spectrum in each voxel (see Figures 8, 12). The presented method of spectrum separation overcomes a significant limitation of MRSI-based diagnosis: although metabolite concentrations correlate with histological findings, the relationship is degraded by significant variability due to partial volume coverage.

By applying the NMF algorithm to 20 ^{1}H MRS scans of brain tumors, our study demonstrates that one can rapidly identify metabolically meaningful spectral patterns. Using the model with two basic sources, i.e. normal and tumor (constituent spectra), the extracted spectrum with highest CNI is considered a tumor spectrum while the spectrum with lowest CNI is considered normal. The assignment is consistent with the typical

patterns of MRSI that tumor spectrum is characterized by an increase of Cho and a reduced NAA as compared to the normal tissue voxel.

In the cases with clear lactate/lipid peaks, the third constituent corresponds to high-lipid tumor region (2 out of 20), provided that the corresponding frequency range is included. By incorporating this additional lipid/lactate information into the current classification methodology, our proposed method shows great potential in differentiating necrotic tissues from residual tumor tissues, and further improve classification accuracy.

Moreover, we performed a validation study to demonstrate the physical relevance of the NMF decomposition. We showed in the phantom study that the method correctly decomposes the observed data into constituent spectra corresponding to the different solutions with their specific metabolite concentrations. It validated the interpretation of abundance estimates $\boldsymbol{A}$ as partial volume fraction and established confidence intervals for its estimates. In addition, we have confirmed the physiological and clinical relevance of the extracted spectra $\boldsymbol{S}$ by correlating the analysis results with pathologically proven tumor grades from 20 patients. Despite known tumor heterogeneity we have shown an improved correlation of tumor grade with spectral patterns (Cho level versus NAA level) supporting our hypothesis that some variability is due to the partial volume effect. We have quantified the limitations of the method by using simulation and found that a minimum SNR of 4dB is required for at least a fraction of relevant voxels. Taken together, the results indicate that MRSI in combination with the proposed spectrum separation method may be useful in defining tumor margins for treatment planning of radiation therapy (112) or surgical resection.

In addition to the traditional NMF algorithm proposed in the study which requires all the data to be positive, this thesis also developed the data processing routine by using a generalize factorization algorithm called semi-NMF. The approach allows the data matrix to have mixed signs, which is better suited for MRSI data as compared to the conventional NMF algorithm. When applied to the same phantom data, the algorithm correctly decomposes the observed data into constituent spectra that correspond to the different solutions with their specific metabolite concentrations. These results indicate that if real absorption spectrum has sufficient quality and can be used for the analysis, semi-NMF can avoid the nonlinearity introduced by using absolute spectra and has the potential in further improving spectrum separation of MRSI.

To certain extent, advances in modern medicine are dependent largely on the advances of new technologies including modern medical imaging technologies. Novel mathematical algorithms are playing an important role in improving the diagnostic value of medical modality by obtaining more and better information from given medical imaging. Different algorithms have been developed with the intent to improve the diagnostic value of MRSI in the past two decades since the emerge of this promising imaging technology. Although many algorithms were reported to be able to successfully decompose MRSI spectra, few has proved the physical reality of the mathematical decomposition and its relevant to disease or health status. In this thesis, we validated the physiological and clinical relevance of components extracted from brain tumor MRSI spectra indicating that decomposition of brain tumor MRSI via NMF is not only applicable but also physiologically and clinically meaningful. It suggests that mathematical decomposition of MRSI spectra can extract physically relevant components

thus provide doctors with more clinical information and improve the effectiveness of MRSI as a diagnostic tool.

11.2 Future Work

In this thesis, the quantification of the abundance estimates shows that the spectrum separation methods are limited by upward and downward estimation bias for low and high volume fractions. There are at least two possible reasons:

1) The violation of the linear assumption for NMF algorithm by using absolute operation.

The semi-NMF algorithm proposed in this study indicates the great potential in eliminating the nonlinear distortions to the spectra because it allows negative values, and consequently using real spectrum for the analysis. Further research will continue exploring advanced phase correction solutions. It may include sophisticated pulse and sequence design to better compensate equipment instability and to improve magnetic field homogeneity; novel algorithms to improve the efficacy of the phase correction routine and specialized computational approaches to obtain satisfactory real spectra.

2) Cr signal attenuation introduced by magnetic transfer (MT) effect during the phantom experiment.

Cr is a chemical which will have considerable MT effect in the NMR experiment, particularly in solute experiment. To quantify the concentration modification by MT effect is quite complicated and will need advanced sequence design and phantom experiments to monitor the metabolite attenuation. To overcome its effects, instead of Cr more reliable chemicals should be used to perform the quantification analysis. It will need further investigation of the biochemistry of the metabolites and their properties in the magnetic fields.

Additional future work should also include exploring wider implications of current spectrum separation methods. This thesis is focused on the clinical utility of spectrum separation for MRSI of brain tumors. However, it may have other implications since this method is applicable to many spectroscopic modalities and multiple organ systems. One example is prostate cancer. The spectra acquired from prostate cancer have different character compared to brain cancer. Instead of using increased Cho peak at 3.2ppm as the biomarker in the brain cancer, elevated Citrate at 2.6ppm is often used biomarker to access the abnormality of the spectra in prostate cancer. The spatial resolution in prostate tumor scan is around 0.25cc (is 1/4 of the 1cc resolution of brain tumor spectra). This low spatial resolution significantly decreases SNR and therefore limits the potential of MRSI-based diagnosis for prostate cancer. The spectrum separation method was developed based on the hypothesis that mixed spectra lead to deleterious spectral variability. The physiological and clinical relevance of the decomposition confirmed in this study indicate that the spectrum separation approach have the potential in decreasing spectral variability and as a result an improved effectiveness of MRSI as a diagnostic tool for prostate cancer.

Another possible application of the spectrum separation method is for longitudinal studies which has become a popular research field. The extracted constituent spectra are particularly useful in monitoring tumor responses to treatments. And accurate abundance estimates can be helpful in delineating tumor extents for the planning of radiation or surgical treatment. On the other hand, applying spectrum separation to longitudinal data is another interesting way to further test the robustness of the algorithm.

11.3 Final Words

The ultimate goal of spectral analysis is to determine accurate estimates of metabolites peak areas that reflect metabolite concentrations. The increasing sophistication of *in vivo* MRS processing methods have been significantly improving the quality of the spectra and changing the traditional interpretation of "MRS" from "Most Random Spike" to "Mainly Real Signal". The use of *in vivo* MRS studies will continue to increase in the coming years due to technological improvements, including the increased availability of higher-field strength MR instruments. It is expected that advances in pulse sequence design, analysis methods, and the use of high magnetic fields will continue to occur. With this potential for improving spectral SNR and resolution using high field MR scanners, the spectrum separation approach will show increased accuracy in capturing the partial volume effect, and therefore increase the efficiency of the spectrum separation as a tool for MRSI analysis. We believe that with all this, there will be ample opportunities to turn MRS into "Manifestly Rich Signatures".

Bibliography

1. Sajda P, Du S, Brown TR, Stoyanova R, Shungu DC, Mao X, Parra LC. Nonnegative matrix factorization for rapid recovery of constituent spectra in magnetic resonance chemical shift imaging of the brain. IEEE Trans Med Imaging 2004;23(12):1453-1465.

2. Su Y, Thakur S, Huang W, Du S, Sajda P, Parra L. Spectrum separation resolves partial volume effect in MRSI. Annual Fall Meeting of the BME Society. Baltimore, MD.; 2005; P1.149.

3. Su Y, Thakur S, Karimi S, Du S, Sajda P, Huang W, Parra L. Spectrum Separation for Brain Tumor MRSI: Validation of Extracted Spectra and Abundance Estimates. Annual Fall Meeting of the BME Society. Saint Louis, MO, USA; 2008; P5.2

4. Su Y, Thakur S, Sasan K, Du S, Sajda P, Huang W, Parra L. Spectral Separation Resolves Partial Volume Effect of MRSI as Demonstrated on Brain Tumor Scans. ISMRM Workshop on Data Processing for MR Spectroscopy and Imaging. Warrenton, Virginia 2006.

5. Su Y, Thakur S, Sasan K, Du S, Sajda P, Huang W, Parra L. Spectral Separation Resolves Partial Volume Effect in MRSI: A Validation Study. Bioengineering Conference, NEBC '07, IEEE 33rd Annual Northeast. Long Island, NY; 2007.

6. Su Y, Thakur SB, Karimi S, Du S, Sajda P, Huang W, Parra LC. Spectrum separation resolves partial-volume effect of MRSI as demonstrated on brain tumor scans. NMR in biomedicine 2008;21(10):1030-1042.

7. Thakur S, Su Y, Sasan K, Du S, Sajda P, Huang W, Parra L. Spectral Separation Analyses of Proton MRSI Data: Validation with Tumor Grade of Brain Glioma. Proceedings of ISMRM 14th Scientific Meeting & Exhibition. Seattle, WA, USA; 2006. p 64.

8. Kurki T, Lundbom N, Kalimo H, Valtonen S. MR classification of brain gliomas: value of magnetization transfer and conventional imaging. Magnetic resonance imaging 1995;13(4):501-511.

9. Vogl TJ, Friebe CE, Balzer T, Mack MG, Steiner S, Schedel H, Pegios W, Lanksch W, Banzer D, Felix R. [Diagnosis of cerebral metastasis with standard dose gadobutrol vs. a high dose protocol. Intraindividual evaluation of a phase II high dose study]. Der Radiologe 1995;35(8):508-516.

10. Ringertz HG. MRI: worth a Nobel Prize? J Am Coll Radiol 2005;2(1):82-85.

11. Alesch F, Pappaterra J, Trattnig S, Koos WT. The role of stereotactic biopsy in radiosurgery. Acta neurochirurgica 1995;63:20-24.

12. Dean BL, Drayer BP, Bird CR, Flom RA, Hodak JA, Coons SW, Carey RG. Gliomas: classification with MR imaging. Radiology 1990;174(2):411-415.

13. Earnest Ft, Kelly PJ, Scheithauer BW, Kall BA, Cascino TL, Ehman RL, Forbes GS, Axley PL. Cerebral astrocytomas: histopathologic correlation of MR and CT contrast enhancement with stereotactic biopsy. Radiology 1988;166(3):823-827.

14. Yu X, Liu Z, Tian Z, Li S, Huang H, Xiu B, Zhao Q, Liu L, Jing W. Stereotactic biopsy for intracranial space-occupying lesions: clinical analysis of 550 cases. Stereotactic and functional neurosurgery 2000;75(2-3):103-108.

15. Brown TR, Kincaid BM, Ugurbil K. NMR chemical shift imaging in three dimensions. Proceedings of the National Academy of Sciences of the United States of America 1982;79(11):3523-3526.

16. Central Brain Tumor Registry of the United States, Statistical report: primary brain tumors in the United States, 1998–2002. Chicago: Central Brain Tumor Registry of the United States; 2005.

17. SEER Cancer Statistics Review, 1975-2006. National Cancer Institute. Bethesda, MD.

18. CA: A Cancer Journal for Clinicians Cancer Statistics January/February 2007;57(Number 1):59.

19. Smirniotopoulos JG. The new WHO classification of brain tumors. Neuroimaging Clin N Am 1999;9(4):595-613.

20. Matthews PM, Wylezinska M, Cadoux-Hudson T. Novel approaches to imaging brain tumors. Hematology/oncology clinics of North America 2001;15(4):609-630.

21. Rosen Y, Lenkinski RE. Recent advances in magnetic resonance neurospectroscopy. Neurotherapeutics 2007;4(3):330-345.

22. Golder W. Magnetic resonance spectroscopy in clinical oncology. Onkologie 2004;27(3):304-309.

23. Bernstein M, Parrent AG. Complications of CT-guided stereotactic biopsy of intra-axial brain lesions. Journal of neurosurgery 1994;81(2):165-168.

24. Chang L, McBride D, Miller BL, Cornford M, Booth RA, Buchthal SD, Ernst TM, Jenden D. Localized in vivo 1H magnetic resonance spectroscopy and in vitro analyses of heterogeneous brain tumors. J Neuroimaging 1995;5(3):157-163.

25. McBride DQ, Miller BL, Nikas DL, Buchthal S, Chang L, Chiang F, Booth RA. Analysis of brain tumors using 1H magnetic resonance spectroscopy. Surgical neurology 1995;44(2):137-144.

26. Usenius JP, Kauppinen RA, Vainio PA, Hernesniemi JA, Vapalahti MP, Paljarvi LA, Soimakallio S. Quantitative metabolite patterns of human brain tumors: detection by 1H NMR spectroscopy in vivo and in vitro. Journal of computer assisted tomography 1994;18(5):705-713.

27. Usenius JP, Vainio P, Hernesniemi J, Kauppinen RA. Choline-containing compounds in human astrocytomas studied by 1H NMR spectroscopy in vivo and in vitro. Journal of neurochemistry 1994;63(4):1538-1543.

28. Simmons ML, Frondoza CG, Coyle JT. Immunocytochemical localization of N-acetyl-aspartate with monoclonal antibodies. Neuroscience 1991;45(1):37-45.

29. Meyerand ME, Pipas JM, Mamourian A, Tosteson TD, Dunn JF. Classification of biopsy-confirmed brain tumors using single-voxel MR spectroscopy. Ajnr 1999;20(1):117-123.

30. Negendank WG, Sauter R, Brown TR, Evelhoch JL, Falini A, Gotsis ED, Heerschap A, Kamada K, Lee BC, Mengeot MM, Moser E, Padavic-Shaller KA, Sanders JA, Spraggins TA, Stillman AE, Terwey B, Vogl TJ, Wicklow K, Zimmerman RA. Proton magnetic resonance spectroscopy in patients with glial tumors: a multicenter study. Journal of neurosurgery 1996;84(3):449-458.

31. Miller BL. A review of chemical issues in 1H NMR spectroscopy: N-acetyl-L-aspartate, creatine and choline. NMR in biomedicine 1991;4(2):47-52.

32. Kreis R, Ernst T, Ross BD. Development of the human brain: in vivo quantification of metabolite and water content with proton magnetic resonance spectroscopy. Magn Reson Med 1993;30(4):424-437.

33. Howe FA, Barton SJ, Cudlip SA, Stubbs M, Saunders DE, Murphy M, Wilkins P, Opstad KS, Doyle VL, McLean MA, Bell BA, Griffiths JR. Metabolic profiles of human brain tumors using quantitative in vivo 1H magnetic resonance spectroscopy. Magn Reson Med 2003;49(2):223-232.

34. Majos C, Alonso J, Aguilera C, Serrallonga M, Perez-Martin J, Acebes JJ, Arus C, Gili J. Proton magnetic resonance spectroscopy ((1)H MRS) of human brain tumours: assessment of differences between tumour types and its applicability in brain tumour categorization. European radiology 2003;13(3):582-591.

35. Yeung DK, Yang WT, Tse GM. Breast cancer: in vivo proton MR spectroscopy in the characterization of histopathologic subtypes and preliminary observations in axillary node metastases. Radiology 2002;225(1):190-197.

36. Swanson MG, Vigneron DB, Tran TK, Sailasuta N, Hurd RE, Kurhanewicz J. Single-voxel oversampled J-resolved spectroscopy of in vivo human prostate tissue. Magn Reson Med 2001;45(6):973-980.

37. Sander J. (1995) Magnetic resonance spectroscopy. In: Orrison WW, Lewine JD, Sanders JA, Harthshorne MF (eds) Functional brain imaging Mosby, St Louis; 1995. p 419–467.

38. Kugel H, Heindel W, Ernestus RI, Bunke J, du Mesnil R, Friedmann G. Human brain tumors: spectral patterns detected with localized H-1 MR spectroscopy. Radiology 1992;183(3):701-709.

39. Preul MC, Caramanos Z, Collins DL, Villemure JG, Leblanc R, Olivier A, Pokrupa R, Arnold DL. Accurate, noninvasive diagnosis of human brain tumors by using proton magnetic resonance spectroscopy. Nature medicine 1996;2(3):323-325.

40. Hugg JW, Duijn JH, Matson GB, Maudsley AA, Tsuruda JS, Gelinas DF, Weiner MW. Elevated lactate and alkalosis in chronic human brain infarction observed by 1H and 31P MR spectroscopic imaging. J Cereb Blood Flow Metab 1992;12(5):734-744.

41. De Edelenyi FS, Rubin C, Esteve F, Grand S, Decorps M, Lefournier V, Le Bas JF, Remy C. A new approach for analyzing proton magnetic resonance spectroscopic images of brain tumors: nosologic images. Nature medicine 2000;6(11):1287-1289.

42. McKnight TR, Noworolski SM, Vigneron DB, Nelson SJ. An automated technique for the quantitative assessment of 3D-MRSI data from patients with glioma. J Magn Reson Imaging 2001;13(2):167-177.

43. Nelson SJ. Multivoxel magnetic resonance spectroscopy of brain tumors. Molecular cancer therapeutics 2003;2(5):497-507.

44. Howe FA, Opstad KS. 1H MR spectroscopy of brain tumours and masses. NMR in biomedicine 2003;16(3):123-131.

45. Fulham MJ, Bizzi A, Dietz MJ, Shih HH, Raman R, Sobering GS, Frank JA, Dwyer AJ, Alger JR, Di Chiro G. Mapping of brain tumor metabolites with proton MR spectroscopic imaging: clinical relevance. Radiology 1992;185(3):675-686.

46. Furuya S, Naruse S, Ide M, Morishita H, Kizu O, Ueda S, Maeda T. Evaluation of metabolic heterogeneity in brain tumors using 1H-chemical shift imaging method. NMR in biomedicine 1997;10(1):25-30.

47. Segebarth CM, Baleriaux DF, Luyten PR, den Hollander JA. Detection of metabolic heterogeneity of human intracranial tumors in vivo by 1H NMR spectroscopic imaging. Magn Reson Med 1990;13(1):62-76.

48. Hofmann L, Slotboom J, Jung B, Maloca P, Boesch C, Kreis R. Quantitative 1H-magnetic resonance spectroscopy of human brain: Influence of composition and parameterization of the basis set in linear combination model-fitting. Magn Reson Med 2002;48(3):440-453.

49. Preul MC, Caramanos Z, Leblanc R, Villemure JG, Arnold DL. Using pattern analysis of in vivo proton MRSI data to improve the diagnosis and surgical management of patients with brain tumors. NMR in biomedicine 1998;11(4-5):192-200.

50. Liang Z, Lauterbur P. Principles of Magnetic Resonance Imaging, A signal processing perspective: Wiley-IEEE Press; 2000.

51. Liang Z, Lauterbur P. Mathematical Fundamentals. In: Liang Z, Lauterbur P, editors. Principles of Magnetic Resonance Imaging: A signal processing perspective. New York: IEEE Press; 2000. p 13-51.

52. Mierisova S, Ala-Korpela M. MR spectroscopy quantitation: a review of frequency domain methods. NMR in biomedicine 2001;14(4):247-259.

53. Vanhamme L, Sundin T, Hecke PV, Huffel SV. MR spectroscopy quantitation: a review of time-domain methods. NMR in biomedicine 2001;14(4):233-246.

54. in 't Zandt H, van Der Graaf M, Heerschap A. Common processing of in vivo MR spectra. NMR in biomedicine 2001;14(4):224-232.

55. Hagberg G. From magnetic resonance spectroscopy to classification of tumors. A review of pattern recognition methods. NMR in biomedicine 1998;11(4-5):148-156.

56. el-Deredy W. Pattern recognition approaches in biomedical and clinical magnetic resonance spectroscopy: a review. NMR in biomedicine 1997;10(3):99-124.

57. van der Veen JW, de Beer R, Luyten PR, van Ormondt D. Accurate quantification of in vivo 31P NMR signals using the variable projection method and prior knowledge. Magn Reson Med 1988;6(1):92-98.

58. Provencher SW. Automatic quantitation of localized in vivo 1H spectra with LCModel. NMR in biomedicine 2001;14(4):260-264.

59. Stoyanova R, Brown TR. NMR spectral quantitation by principal component analysis. NMR in biomedicine 2001;14(4):271-277.

60. Kuesel AC, Stoyanova R, Aiken NR, Li CW, Szwergold BS, Shaller C, Brown TR. Quantitation of resonances in biological 31P NMR spectra via principal component analysis: potential and limitations. NMR in biomedicine 1996;9(3):93-104.

61. Menze BH, Lichy MP, Bachert P, Kelm BM, Schlemmer HP, Hamprecht FA. Optimal classification of long echo time in vivo magnetic resonance spectra in the detection of recurrent brain tumors. NMR in biomedicine 2006;19(5):599-609.

62. Nuzillard D, Bourg S, Nuzillard J. Model-free analysis of mixtures by NMR using blind source separation. J Magn Reson 1998;133(2):358-363.

63. Ladroue C, Howe FA, Griffiths JR, Tate AR. Independent component analysis for automated decomposition of in vivo magnetic resonance spectra. Magn Reson Med 2003;50(4):697-703.

64. Shimizu H, Kumabe T, Shirane R, Yoshimoto T. Correlation between choline level measured by proton MR spectroscopy and Ki-67 labeling index in gliomas. Ajnr 2000;21(4):659-665.

65. Ahn J, Kim S, Oh J, Choi S. Multiple nonnegative matrix factorization of dynamic PET images. ACCV; 2004.

66. Carmona-Saez P, Pascual-Marqui RD, Tirado F, Carazo JM, Pascual-Montano A. Biclustering of gene expression data by Non-smooth Non-negative Matrix Factorization. BMC bioinformatics 2006;7:78.

67. Cho YC, Choi S. Nonnegative features of spectro-temporal sounds for classification. Pattern Recognition Letters 2005;26:1327–1336.

68. Guillamet D, Schiele B, Vitria J. Analyzing non-negative matrix factorization for image classification. 16th International Conference on Pattern Recognition (ICPR' 02). Volume 2. Quebec City, Canada; 2002. p 116-119.

69. Guillamet D, Vitria J. Classifying faces with nonnegative matrix factorization. Proc of the Fifth Catalan Conference for Artificial Intelligence. Castello de la Plana, Spain; 2002.

70. Guillamet D, Vitria J, Schiele B. Introducing a weighted non-negative matrix factorization for image classification Pattern Recognition Letters 2003;24(14):2447-2454.

71. Lee DD, Seung HS. Learning the parts of objects by non-negative matrix factorization. Nature 1999;401(6755):788-791.

72. Lee JS, Lee DD, Choi S, Lee DS. Application of nonnegative matrix factorization to dynamic positron emission tomography. Third International Conference on

Independent Component Analysis and Blind Signal Separation. San Diego, CA; 2001. p 556–562.

73. Li H, Adali T, Wang DEW. Non-negative matrix factorization with orthogonality constraints for chemical agent detection in raman spectra. IEEE Workshop on Machine Learning for Signal Processing. Mystic, USA; 2005.

74. Liu W, Zheng N. Non-negative matrix factorization based methods for object recognition. Pattern Recognition Letters 2004;25(8):893–897.

75. Okun O, Priisalu H. Fast Nonnegative Matrix Factorization and Its Application for Protein Fold Recognition. EURASIP Journal on Applied Signal Processing, 2006, Article ID 71817, 8 pages 2006.

76. Pascual-Montano A, Carazo JM, Kochi K, Lehmann D, Pascual-Marqui RD. Nonsmooth nonnegative matrix factorization (nsNMF). IEEE transactions on pattern analysis and machine intelligence 2006;28(3):403-415.

77. Shahnaz F, Berry M, Pauca P, Plemmons R. Document clustering using non-negative matrix factorization. Information Processing and Management 2006;42(2):373-386.

78. Spratling MW. Learning image components for object recognition. Journal of Machine Learning Research 2006;7:793–815.

79. Wang Y, Jia Y, Hu C, Turk M. Non-negative matrix factorization framework for face recognition. Int J Pattern Recognition Artif Intell 2005;19(4):495–511.

80. Sajda P, Du S, Brown TR, Parra LC, Stoyanova R. Recovery of constituent spectra in 3d chemical shift imaging using nonnegative matrix factorization. Fourth International Symposium on Independent Component Analysis and Blind Signal Separation. Nara, Japan; 2003. p 71–76.

81. Sajda P, Du S, Parra LC. Recovery of constituent spectra using non-negative matrix factorization. Proceedings of SPIE—Wavelets: Applications in Signal and Image Processing. Volume 5207; 2003. p 321–331.

82. Dhillon IS, Modha DM. Concept decompositions for large sparse text data using clustering. Mach Learn J 2001;42:143–175.

83. Brunet JP, Tamayo P, Golub TR, Mesirov JP. Metagenes and molecular pattern discovery using matrix factorization. Proceedings of the National Academy of Sciences of the United States of America 2004;101(12):4164-4169.

84. Rao N, Shepherd SJ, Yao D. Extracting characteristic patterns from genome—wide expression data by non-negative matrix factorization. Proceedings of the 2004 IEEE Computational Systems Bioinformatics Conference (CSB 2004). Stanford, CA; 2004.

85. Anttila P, Paatero P, Tapper U, Järvinen O. Source identification of bulk wet deposition in Finland by positive matrix factorization. Atmospheric Environment 1995;29:1705-1718.

86. Paatero P, Tapper U. Positive matrix factorization: A non-negative factor model with optimal utilization of error estimates of data values. Environmetrics 1994;5:111–126.

87. Dhillon IS, Sra S. Generalized Nonnegative Matrix Approximations with Bregman Divergences. Neural Information Processing Systems (NIPS). Vancouver, Canada; 2005.

88. Lee DD, Seung HS. Algorithms for non-negative matrix factorization. Advances in Neural Information Processing Systems 13 MIT Press, 2001:556-562.

89. CBTRUS 2007 - 2008. Primary Brain Tumors in the United States Statistical Report 2000 - 2004. Central Brain Tumor Registry of the United States.

90. Yan H. Signal Processing for Magnetic Resonance Imaging and Spectroscopy: Taylor & Francis, Inc.; 2002.

91. Laudadio T, Pels P, De Lathauwer L, Van Hecke P, Van Huffel S. Tissue segmentation and classification of MRSI data using canonical correlation analysis. Magn Reson Med 2005;54(6):1519-1529.

92. Brown TR, Stoyanova R. NMR spectral quantitation by principal-component analysis. II. Determination of frequency and phase shifts. Journal of magnetic resonance 1996;112(1):32-43.

93. Witjes H, Melssen WJ, in 't Zandt HJ, van der Graaf M, Heerschap A, Buydens LM. Automatic correction for phase shifts, frequency shifts, and lineshape distortions across a series of single resonance lines in large spectral data sets. J Magn Reson 2000;144(1):35-44.

94. Sajda P. Machine Learning for Detection and Diagnosis of Disease. Annu Rev Biomed Eng 2006;8:537-565

95. Jolliffe IT. Principal Component Analysis. New York: SpringerVerlag; 1986.

96. Mason SJ, Graham NE. Areas beneath the relative operating characteristics (ROC) and relative operating levels (ROL) curves: Statistical significance and interpretation. Quarterly Journal of the Royal Meteorological Society 2002;128:2145-2166.

97. Mooney C, Duval R. Bootstrapping: A Nonparametric Approach to Statistical Inference. Newbury Park, CA: SAGE Publications; 1993.

98. Polikar R. Bootstrap-inspired techniques in computational intelligence: ensemble of classifiers for incremental learning, data fusion and missing feature analysis. IEEE Signal Processing Magazine 2007;24(4):59-72.

99. McKnight TR, von dem Bussche MH, Vigneron DB, Lu Y, Berger MS, McDermott MW, Dillon WP, Graves EE, Pirzkall A, Nelson SJ. Histopathological validation of a three-dimensional magnetic resonance spectroscopy index as a predictor of tumor presence. Journal of neurosurgery 2002;97(4):794-802.

100. Park I, Tamai G, Lee MC, Chuang CF, Chang SM, Berger MS, Nelson SJ, Pirzkall A. Patterns of recurrence analysis in newly diagnosed glioblastoma multiforme after three-dimensional conformal radiation therapy with respect to pre-radiation therapy magnetic resonance spectroscopic findings. International journal of radiation oncology, biology, physics 2007;69(2):381-389.

101. DeLong ER, DeLong DM, Clarke-Pearson DL. Comparing the areas under two or more correlated receiver operating characteristic curves: A nonparametric approach. Biometrics 1988;44:837-845.

102. MuCullagh P, Nelder JA. Generalized Linear Models: Chapman & Hall; 1990.

103. Dobson AJ. An Introduction to Generalized Linear Models: CRC Press; 1990.

104. Collett D. Modelling Binary Data: Chapman & Hall/CRC Press; 2002.

105. Ding C, Li T, Jordan M. Convex and Semi-Nonnegative Matrix Factorizations: Lawrence Berkeley National Laboratory, University of California, Berkeley; 2006.

106. Wolff SD, Balaban RS. Magnetization transfer contrast (MTC) and tissue water proton relaxation in vivo. Magn Reson Med 1989;10(1):135-144.

107. de Graaf RA, van Kranenburg A, Nicolay K. Off-resonance metabolite magnetization transfer measurements on rat brain in situ. Magn Reson Med 1999;41(6):1136-1144.

108. Helms G, Frahm J. Magnetization transfer attenuation of creatine resonances in localized proton MRS of human brain in vivo. NMR in biomedicine 1999;12(8):490-494.

109. Kreis R, Boesch C. Localized 1H-MRS without water saturation: Techniques and initial results for human brain and muscle. Proceeding of the VI ISMRM meeting; Sydney April;1998. p 24.

110. Leibfritz D, Dreher W. Magnetization transfer MRS. NMR in biomedicine 2001;14(2):65-76.

111. Schneider J, Fekete E, Neubauer S, Haase A, von Kienlin A. Visibility of total creatine by 1H-MRS in perfused rat hearts. Proceedings of the VIII ISMRM Meeting; Glasgow. April; 1999. p 591.

112. Graves EE, Pirzkall A, Mcknight TR, Vigneron DB, Larson DA, Verhey LJ, Mcdermott M, Chang S, Nelson SJ. Use of Proton Magnetic Resonance Spectroscopic Imaging Data in Planning Focal Radiation Therapies for Brain Tumors. Image Anal Stereol 2002;21:69-76.